J. Fluid Mech. (2005), *vol.* 545, *pp.* 397–426. © 2005 Cambridge University Press
doi:10.1017/S0022112005006907 Printed in the United Kingdom

The drag on a microcantilever oscillating near a wall

By R. J. CLARKE[1], S. M. COX[2], P. M. WILLIAMS[3] AND O. E. JENSEN[1]

[1]Division of Applied Mathematics, School of Mathematical Sciences, University of Nottingham, University Park, Nottingham NG7 2RD, UK

[2]School of Mathematical Sciences, University of Adelaide, Adelaide 5005, Australia

[3]Laboratory of Biophysics and Surface Analysis, School of Pharmacy, University of Nottingham, University Park, Nottingham NG7 2RD, UK

(Received 19 August 2004 and in revised form 6 June 2005)

Motivated by devices such as the atomic force microscope, we compute the drag experienced by a cylindrical body of circular or rectangular cross-section oscillating at small amplitude near a plane wall. The body lies parallel to the wall and oscillates normally to it; the body is assumed to be long enough for the dominant flow to be two-dimensional. The flow is parameterized by a frequency parameter γ^2 (a Strouhal number) and the wall–body separation Δ (scaled on body radius). Numerical solutions of the unsteady Stokes equations obtained using finite-difference computations in bipolar coordinates (for circular cross-sections) and boundary-element computations (for rectangular cross-sections) are used to determine the drag on the body. Numerical results are validated and extended using asymptotic predictions (for circular cylinders) obtained at all extremes of (γ, Δ)-parameter space. Regions in parameter space for which the wall has a significant effect on drag are identified.

1. Introduction

The leading-order flow generated by an isolated body oscillating at small amplitude with frequency ω, in fluid of density ρ and viscosity μ, is described by the unsteady Stokes equations

$$\rho\frac{\partial \boldsymbol{U}}{\partial t} = -\nabla P + \mu\nabla^2\boldsymbol{U}, \quad \nabla\cdot\boldsymbol{U} = 0, \tag{1.1}$$

where $\boldsymbol{U}$, P are the fluid velocity and pressure, respectively. Unsteady inertial forces confine the diffusion of vorticity away from the surface of the body to a distance of $O(\mathscr{L})$, where $\mathscr{L} = (\mu/(\rho\omega))^{1/2}$. In quasi-steady motion, when $\mathscr{L}$ is large compared to the diameter of the body, the presence of a boundary confining the flow is likely to have a profound effect on the body's motion, consistent with the well-known long-range character of Stokes flows. For two-dimensional flows in particular, the drag experienced by the body is likely to depend at leading order on its distance from the boundary (albeit logarithmically when the body is far from the boundary). At high frequencies, even though viscous effects may be confined to the immediate neighbourhood of any solid surfaces, it is less obvious what role external boundaries may play. This paper addresses this fundamental issue for two-dimensional flows, by determining the drag on an oscillating body in the presence of a rigid wall.

There are numerous applications in which such considerations are significant, including ultrasonics, electroacoustics and microelectromechanical systems. The motivation of the present study is the atomic force microscope (AFM), a widely used device in which a small cantilever oscillates in close proximity to a solid surface, often at high frequencies, in response to external driving (in so-called tapping mode) or thermal fluctuations of the surrounding fluid (either liquid or gas). The cantilever, which is much greater in length than in width, and which typically operates less than a width away from the substrate, may be assumed to generate a flow that is predominantly two-dimensional away from its ends. Deflections of the cantilever are measured using a reflected laser beam, from which the loading on the cantilever can be inferred once the cantilever's spring constant is accurately known. However, determining the spring constant for a given cantilever is a non-trivial exercise and a common calibration technique involves analysis of the spectrum of the cantilever under thermal driving. The influence of a nearby wall shows clearly in these spectra. Benmouna & Johannsmann (2002) and Nnebe & Schneider (2004), for example, show how the resonant peaks of the thermal spectra flatten as the cantilever approaches the wall, although a number of effects (not just hydrodynamic) may be responsible for this behaviour. Current models of the AFM either do not account explicitly for hydrodynamic interactions between the cantilever and the wall (e.g. Sader 1998) or are restricted to quasi-steady approximations (e.g. Vinogradova *et al.* 2001; Alcaraz 2002). One contribution of the present study is to provide improved understanding of the role of a nearby solid boundary on the hydrodynamic load placed on an oscillating cantilever over a wide range of frequencies. This should not only aid the calibration effort, but also provide a means to distinguish between hydrodynamic loading and interactions between the wall and cantilever tip of non-hydrodynamic origin.

Numerous workers have addressed the problem of the unsteady drag on an isolated body oscillating at small amplitude following Stokes' (1851) treatment of a cylinder and sphere (see Rosenhead 1963). His expression for the drag on an oscillating sphere may be decomposed into the steady (Stokes) drag, an added-mass term and a history-dependent term often called the Basset force (Basset 1888). Lawrence & Weinbaum (1986, 1988) demonstrated that this decomposition does not carry over to axially oscillating spheroids, for which the body's non-spherical geometry produces a complicated fourth drag component. Despite its complexity, a good approximation could be made to this additional drag component by taking a suitable linear combination of the Basset force and the first inertial correction to the steady Stokes drag. Although this *ad hoc* approximation was developed from results for axially oscillating spheroids, its applicability has been shown to be quite general. Pozrikidis (1989*a*) demonstrated its success in approximating the drag on a transversely oscillating spheroid, and Loewenberg (1993) showed that the Lawrence & Weinbaum (1988) result could also reliably approximate the drag on axially and transversely oscillating cylinders, provided that they have moderate aspect ratio. Lovalenti & Brady (1993) showed how both unsteady and weak convective inertia contribute to the drag on an impulsively moving sphere.

Numerical methods have been employed for geometrically more complex bodies. Both Pozrikidis (1989*a*) and Loewenberg (1993) determined the full oscillatory flow generated by an oscillating body using numerical methods exploiting the unsteady Stokeslet. (Pozrikidis 1989*a* gives the three-dimensional oscillatory Stokeslet; Avudainayagam & Geetha 1993, 1995 give the two-dimensional Stokeslet for oscillatory and impulsive forcing respectively.) Pozrikidis (1989*a*) used a singularity

method to determine the flow generated by oscillations of a solid sphere, a spherical drop and a spheroid, and a boundary-integral method (Pozrikidis 1989*b*) to compute the flow generated by oscillating spheroids, dumbbells and biconcave disks. One of the main features of these results is the appearance of viscous eddies on the surface of the bodies, which eventually detach and dissipate in the bulk flow. Smith (1995, 1997) described the mechanism of flow reversal in some detail. A boundary-integral formulation was adopted to investigate the flows generated by axial (Loewenberg 1994*b*) and transverse (Loewenberg 1994*a*) oscillations of a finite-length cylinder, which were shown to exhibit qualitative differences from the smooth-body results produced by Pozrikidis (1989*a*). An alternative boundary-integral formulation was developed earlier by Tuck (1969) to describe the two-dimensional flow generated by the transverse oscillations of an infinitely long cylinder with arbitrary cross-section. This integral equation was then solved numerically, using a boundary-element method, for the case of an infinitely thin plate. It was found that the drag exerted on the plate is similar to that felt by a circular cylinder with diameter equal to the plate width, an approximation exploited in the AFM context by Sader (1998) and others. The two-dimensional plate, oscillating in unbounded fluid, had already been studied in its own right by Kanwal (1955), who used elliptic coordinates to represent the flow as an infinite series involving Mathieu functions.

Oscillatory flows generated by isolated disks have been determined using dual integral-equation methods by Davis (1993) and Zhang & Stone (1998). Feng, Ganatos & Weinbaum (1998*a*) treated the mathematically equivalent problem of a disk moving in a Brinkman medium (discussed further below). Tekasakul, Tompson, & Loyalka (1998) provide an overview of oscillatory flows generated by a variety of axisymmetric bodies.

Fewer studies of oscillatory flows have accounted for the presence of nearby walls. Chu & Kim (2002) determined the oscillatory two-dimensional flow around a semi-infinite plate parallel to a wall; they later extended the dual-integral-equation method of Zhang & Stone (1998) to describe a disk undergoing rotational and translation motions above a plane wall (Chu & Kim 2004). Singularity-based methods can be adapted to account for the presence of a wall using the method of images (Pozrikidis 1992). For quasi-steady flows this is a standard and effective strategy: Blake (1971), using Fourier transforms, showed that the image system for a Stokeslet in a plane wall is a second Stokeslet, a dipole and a stresslet (a force-doublet). This compact representation has been incorporated in, for example, slender-body theories for rods near walls (Blake 1974; Russel *et al.* 1977). A finite number of image singularities, appropriately located, can be used to describe flows of considerable geometric complexity, for example the Stokes flow generated by moving one cylinder inside another (Finn & Cox 2001). For oscillatory flows, image methods are less straightforward. As shown by Pozrikidis (1989*a*) in three dimensions and Chu & Kim (2001) in two dimensions, to satisfy no-slip and no-penetration conditions on a wall, an oscillatory Stokeslet must be supplemented with an image system reflected in the wall plus a distribution of singularities along the wall. Smith (1987, 1993), for example, gives the image systems for impulsive two-dimensional Stokeslets and rotlets in the presence of external boundaries. While computations with this method are still feasible (see below), they are more elaborate than in the quasi-steady case.

Brinkman's equation is a model for flow in porous media that is valid at low solid volume fraction (Durlofsky & Brady 1987); it is mathematically equivalent to oscillatory Stokes flow, but with $\mathscr{L}$ interpreted as the Brinkman screening length. Studies of the motion of bodies in a Brinkman medium therefore have relevance

to oscillatory flows. Kim & Russel (1985) examined the flow due to two spheres in a Brinkman medium using the method of reflections and a boundary collocation technique. Feng, Ganatos & Weinbaum (1998*b*) computed the flow due to a translating sphere in the presence of a plane wall, employing a boundary-integral technique that exploits symmetry but requires the solution of integral equations on all solid boundaries. Broday (2002) used a boundary-integral method to determine the drag on a spherical bead near a planar interface between two Brinkman media, while Sugihara-Seki (2004) used a finite-element method to compute the motion of a sphere in a cylindrical tube. The motion of a two-dimensional body in a Brinkman medium near a rigid boundary does not appear to have been studied in any detail.

The linearized momentum equation (1.1) describes the leading-order flow in the limit in which the amplitude of oscillation is small compared to the body diameter. At higher orders, nonlinearities associated with convective inertia lead to steady streaming, which produces irreversible migration of fluid particles over time (Riley 2001). While recognizing that this effect may sometimes be significant experimentally, we do not account for it below.

Since the primary application addressed here is the AFM, involving microcantilevers of micron-scale thickness (although considerably greater length and width), it is prudent to consider the validity of the traditional Navier–Stokes/no-slip hydrodynamic model. One advantage of the AFM over other imaging systems is that it enables biological samples to be investigated in a liquid environment, where hydrodynamic effects are likely to be particularly significant. This work is conducted primarily with such applications in mind. When the cantilever operates far from a substrate, we expect slip at the smooth cantilever surface to be weak (molecular-dynamics simulations show the slip length of room-temperature water to be as low as $O(1\,\mathrm{nm})$ (Thompson & Troian 1997), while experiments suggest the slip length on smooth hydrophobic surfaces is around 20 nm (Cottin-Bizonne *et al.* 2005), much less than the 10 μm cantilever width). However when operating very near a substrate (at imaging distances of 1 μm or less), such as a complex biological interface in a liquid environment, slip effects are likely to be much more significant (as are other effects such as non-uniform topography, interfacial compliance, etc.). For an AFM operating far from a substrate in air at normal temperatures and pressures, the Knudsen number $Kn \approx 0.007$ (the ratio of the molecular mean-free path 70 nm to a typical flow dimension, such as the 10 μm cantilever width), a regime in which Navier–Stokes with a slip condition should be appropriate (Roy *et al.* 2003). However, when operating in air very close to a substrate (at 1 μm or less), $Kn \gtrsim 0.07$, a regime in which slip effects become substantial and the continuum approximation is questionable. The validity of the continuum model for the present problem in this regime was tested by molecular gas dynamics simulations by Gallis & Torczynski (2004). Thus, while the conventional no-slip model provides a useful starting point, we recognize that slip and other effects may limit the validity of the results presented below in certain circumstances.

In this paper we determine the unsteady two-dimensional Stokes flow generated by a cantilever oscillating normal to its axis when it lies parallel to a rigid wall. By prescribing the frequency of the cantilever's motion, we construct a temporal Fourier transform that can later be used to determine, for example, the small-amplitude motion of a microcantilever oscillating in response to thermal fluctuations. We examine two cantilever cross-sections, one circular and the other rectangular, and assume that the dominant flow at any station along the cantilever (away from the ends) is two-dimensional. The governing equations are given in § 2. We compute

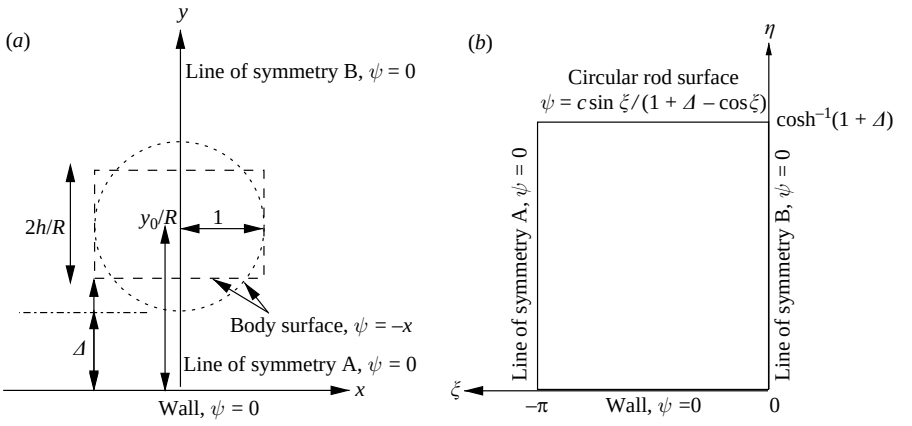

FIGURE 1. (*a*) Cartesian geometry of the flow domain in non-dimensional units in the case of either a circular cantilever (dotted line) or a rectangular cantilever (dashed line). (*b*) Bipolar coordinates (3.1) map the geometry for a circular cantilever to a finite rectangular domain.

the drag numerically, employing finite-difference and boundary-element methods for circular and rectangular cantilevers, respectively (§ 3). We validate and extend these results by developing asymptotic expressions for the drag on a circular cantilever (§ 4). Our coverage of parameter space is systematic (see figure 2 below) and exploits a variety of asymptotic techniques. We show in § 5 how the drag on the cantilever is affected by cantilever shape, oscillation frequency and distance from the wall. Our main conclusions and implications for the operation of the AFM (including the leading-order effects of slip) are discussed in § 6.

2. Model

We consider the two-dimensional unsteady flow satisfying (1.1) generated by small-amplitude vertical oscillatory motion of a cantilever, with either a circular or rectangular cross-section, aligned parallel to an infinite rigid horizontal wall. The circular cantilever has radius R; the rectangular cantilever has horizontal width $2R$ and vertical thickness $2h$. In Cartesian coordinates (x, y), the wall lies at $y = 0$ and the centre of the cantilever lies at $(0, y_0)$ (see figure 1*a*). The cantilever oscillates normal to the wall with frequency ω, with an amplitude of oscillation that is small compared with h and R.

We seek solutions of (1.1) of the form $\boldsymbol{U}(x, y, t) = \mathrm{Re}\left(\boldsymbol{u}(x, y)\mathrm{e}^{\mathrm{i}\omega t}\right)$, $P(x, y, t) = \mathrm{Re}\left(p(x, y)\mathrm{e}^{\mathrm{i}\omega t}\right)$, yielding

$$\mathrm{i}\rho\omega\boldsymbol{u} = -\nabla p + \mu\nabla^2\boldsymbol{u}, \quad \nabla\cdot\boldsymbol{u} = 0, \tag{2.1}$$

which must be solved subject to the boundary conditions

$$\boldsymbol{u}\,|_S = V\,\boldsymbol{j}, \quad \boldsymbol{u}(x, 0) = \boldsymbol{0} \text{ for } -\infty < x < \infty, \quad \boldsymbol{u} \to \boldsymbol{0} \text{ as } |\boldsymbol{x}| \to \infty, \tag{2.2}$$

where $\boldsymbol{j} \equiv (0, 1)$, $V \equiv A\omega$ is the cantilever's maximum speed and S is the cantilever's surface. At small amplitudes we may linearize the boundary conditions on the body or, equivalently, take S to be fixed in (2.2).

As discussed in § 1, in some circumstances it may be necessary to replace the no-slip condition with a Navier-slip condition. Thus on S, for example, where the unit tangent

and normal are $\boldsymbol{t}$ and $\boldsymbol{n}$ respectively, we replace (2.2a) with $\boldsymbol{u}\cdot\boldsymbol{n} = V\,\boldsymbol{j}\cdot\boldsymbol{n}$ and

$$(\boldsymbol{u}\cdot\boldsymbol{t}) - V\,(\boldsymbol{j}\cdot\boldsymbol{t}) = L(R/\mu)\,(\boldsymbol{t}\cdot\boldsymbol{\sigma}\cdot\boldsymbol{n}). \tag{2.3}$$

Here $L \ll 1$ is the dimensionless slip length (scaled on R) and $\boldsymbol{\sigma} = -\boldsymbol{I}p + \mu(\nabla\boldsymbol{u} + \nabla\boldsymbol{u}^T)$ is the stress tensor. A similar condition applies on $y = 0$. We will examine the effect of slip on drag in a couple of instances (see Appendix C below), but otherwise assume no-slip applies.

Rescaling time on ω^{-1}, lengths on R, speeds on V and pressure on $\mu V/R$ recasts (2.1) and (2.2) in the form

$$\mathrm{i}\gamma^2\boldsymbol{u} = -\nabla p + \nabla^2\boldsymbol{u}, \quad \nabla\cdot\boldsymbol{u} = 0, \tag{2.4a}$$

$$\boldsymbol{u}|_S = \boldsymbol{j}, \quad \boldsymbol{u}(x,0) = \boldsymbol{0} \text{ for } -\infty < x < \infty, \quad \boldsymbol{u} \to \boldsymbol{0} \text{ as } |\boldsymbol{x}| \to \infty, \tag{2.4b}$$

where $\gamma^2 = R^2\rho\omega/\mu$; γ^{-1} is a measure of the distance over which vorticity diffuses during an oscillation relative to the cantilever's diameter. The rescaling also generates a second dimensionless parameter, $\Delta = (y_0 - W)/R$, where for circular (or rectangular) cantilevers $W = R$ (or $W = h$); Δ measures the minimum distance between S and the wall, in terms of the cantilever's diameter (see figure 1a). We also define a streamfunction ψ by $\boldsymbol{u} = (\psi_y, -\psi_x)$, where subscripts x and y denote derivatives. Taking the curl of (2.4a) yields

$$\mathrm{i}\gamma^2\nabla^2\psi = \nabla^4\psi, \tag{2.5a}$$

$$\psi(x,0) = 0, \quad \psi_y(x,0) = 0, \quad \psi_x|_S = -1, \quad \psi_y|_S = 0, \quad \psi \to 0 \text{ as } |\boldsymbol{x}| \to \infty. \tag{2.5b}$$

Symmetry of the flow about $x = 0$ means that we need consider the flow only in the quadrant $x \geqslant 0,\ y \geqslant 0$ (figure 1a).

The primary objective of this study is to calculate the drag per unit length D on the cantilever and to assess how this is influenced by Δ, γ and the cantilever's shape. The non-dimensional drag (scaled on μV) is

$$D = \int_S \boldsymbol{j}\cdot\boldsymbol{\sigma}\cdot\boldsymbol{n}\,\mathrm{d}s. \tag{2.6}$$

We now describe the two different numerical techniques that are employed to determine the flow generated by circular and rectangular cantilevers (§ 3) and the asymptotic results that are used to validate and extend the results for circular cantilevers (§ 4).

3. Numerical methods

3.1. *Circular cantilevers: finite-difference method*

When the cantilever is circular, the geometry of the flow lends itself to cylindrical bipolar coordinates (ξ, η), defined by (Jeffery 1921)

$$x = -\frac{c\sin\xi}{\cosh\eta - \cos\xi}, \quad y = \frac{c\sinh\eta}{\cosh\eta - \cos\xi}, \quad c = \sqrt{\Delta(\Delta+2)}. \tag{3.1a–c}$$

In this coordinate system, the flow domain in $x \geqslant 0$ maps to the rectangle $-\pi \leqslant \xi \leqslant 0$, $0 \leqslant \eta \leqslant \eta_1 \equiv \cosh^{-1}(1+\Delta)$ (see figure 1b). However, we gain this finite rectilinear geometry at the cost of losing separability in our governing equation (2.5a), which becomes

$$\mathrm{i}\gamma^2c^2\nabla^2\psi = \nabla^2((\cosh\eta - \cos\xi)^2\nabla^2\psi). \tag{3.2}$$

We discretize (3.2) using a finite-difference method on a uniform mesh and solve the resulting linear system of equations by Gaussian elimination. Following Jeffery (1921) we choose to work with $(\cosh\eta - \cos\xi)\psi/c$ rather than with ψ itself, as this results in a simpler form for the operator and the boundary conditions. As γ is increased the demand for mesh points also increases, to resolve the boundary layers that arise on the cantilever and wall. We obtained solutions for $\gamma \leqslant 30$ on a 200×200 mesh, with convergence verified on a 350×350 mesh and validation provided by comparison with asymptotic results derived in § 4.

3.2. *Rectangular cantilevers: boundary-element method*

For rectangular cantilevers we follow Pozrikidis (1989*b*) and Loewenberg (1994*b*) and use a two-dimensional version of their boundary-integral formulation. For transverse oscillations, Pozrikidis (1989*b*) gives the following first-kind Fredholm equation for the velocity field $\boldsymbol{u}$ in a domain with boundary B and unit outward normal $\boldsymbol{n}$:

$$u_j(\boldsymbol{x}_0) = -\frac{1}{4\pi}\int_B f_i(\boldsymbol{x}) S_{ij}(\hat{\boldsymbol{x}})\,\mathrm{d}s(\boldsymbol{x}), \quad f_i(\boldsymbol{x}) = \sigma_{ik}n_k - \mathrm{i}\gamma^2 u_k x_k n_i, \tag{3.3}$$

where $\boldsymbol{x}_0 \in B$ and $\hat{\boldsymbol{x}} = \boldsymbol{x} - \boldsymbol{x}_0$. The oscillatory free-space Stokeslet S_{ij} is (Avudainayagam & Geetha 1998)

$$S_{ij}(\hat{\boldsymbol{x}}) = \frac{2}{\mathrm{i}\gamma^2}\left(\frac{\delta_{ij}}{\hat{r}^2} - \frac{2\hat{x}_i\hat{x}_j}{\hat{r}^4}\right) - 2K_0(\sqrt{\mathrm{i}}\gamma\hat{r})\left(\delta_{ij} - \frac{\hat{x}_i\hat{x}_j}{\hat{r}^2}\right) - \frac{2K_1(\sqrt{\mathrm{i}}\gamma\hat{r})}{\sqrt{\mathrm{i}}\gamma\hat{r}}\left(\delta_{ij} - \frac{2\hat{x}_i\hat{x}_j}{\hat{r}^2}\right), \tag{3.4}$$

where $\hat{r} = |\hat{\boldsymbol{x}}|$ and $\sqrt{\mathrm{i}} \equiv (1+\mathrm{i})/\sqrt{2}$. High demands on the resolution required to capture viscous boundary layers, and the oscillatory nature of the kernel, both place a practical upper limit on the size of γ and for this reason we also employ a boundary-layer formulation at high frequencies. Here an approximation for the drag on the body is obtained by solving separately for the leading-order inviscid flow, Stokes layers on the solid boundaries and the second-order inviscid flow driven by fluid ejected from the Stokes layers (this secondary inviscid flow makes an $O(\gamma)$ drag contribution, comparable in size to the boundary-layer contribution; note that this linear inviscid flow is distinct from the nonlinear streaming flows that are also generated by Stokes layers, but which we here neglect). The inviscid flows are determined using the standard boundary-integral formulation for the potential flow $\boldsymbol{u} = \nabla\phi$ (Pozrikidis 1996)

$$\phi(\boldsymbol{x}_0) = \frac{1}{\pi}\int_B \boldsymbol{V}'\cdot\boldsymbol{n}\,\ln\hat{r}\,\mathrm{d}s(\boldsymbol{x}) - \frac{1}{\pi}\fint_B \frac{\hat{\boldsymbol{x}}\cdot\boldsymbol{n}}{\hat{r}^2}\,\phi(\boldsymbol{x})\,\mathrm{d}s(\boldsymbol{x}) \tag{3.5}$$

with the second integral taking its Cauchy principal value. Setting $\boldsymbol{V}' = \boldsymbol{j}$ on the cylinder and $\boldsymbol{0}$ on the wall in (3.5) yields an expression for the potential of the primary inviscid flow $\phi^{(1)}$. Boundary layers on the solid surfaces drive a secondary potential flow $\phi^{(2)}$, which can be expressed using (3.5) once we have extracted the value of $\boldsymbol{V}'$ from the boundary-layer flows. Within this asymptotic limit, an approximation for the drag is then given by

$$D = \mathrm{i}\int_B \left(\gamma^2\phi^{(1)} + \gamma\phi^{(2)}\right)\,\mathrm{d}s(\boldsymbol{x}) + \sqrt{\mathrm{i}}\int_{B_v}\gamma\,(v^s - 1)\,\mathrm{d}s(\boldsymbol{x}), \tag{3.6}$$

where B_v represents the vertical sides of the cantilever and $v^s = \phi_y^{(1)}|_{B_v}$ is the slip velocity on these vertical sides. (The corresponding asymptotic expression for the drag on a circular cantilever is derived in § 4.2.2 below.)

Boundary-element methods provide a computational route to solving (3.3) and (3.5) for the modified traction $\boldsymbol{f}(\boldsymbol{x})$ and flow potential $\phi(\boldsymbol{x})$, respectively. Discretizing the cantilever's surface and the wall into N boundary elements, approximating the geometry of the boundary in the kth element with the simple polynomial curve B_k, with mid-point $\boldsymbol{x}_0^{(k)}$, and assuming that $\boldsymbol{f}(\boldsymbol{x})$, $\phi(\boldsymbol{x})$ are constant on each boundary element, we can rewrite (3.3) and (3.5) as the following systems of linear equations, respectively:

$$u_j\left(\boldsymbol{x}_0^{(m)}\right) = -\frac{1}{4\pi}\sum_{k=1}^{N} A_{ij}^k\left(\boldsymbol{x}_0^{(m)}\right) f_i\left(\boldsymbol{x}_0^{(k)}\right), \quad A_{ij}^k\left(\boldsymbol{x}_0^{(m)}\right) = \int_{B_k} S_{ij}\left(\boldsymbol{x}, \boldsymbol{x}_0^{(m)}\right) \mathrm{d}s(\boldsymbol{x}), \tag{3.7a}$$

$$\phi\left(\boldsymbol{x}_0^{(m)}\right) = \frac{1}{\pi}\sum_{k=1}^{N}\left((\boldsymbol{V}'\cdot\boldsymbol{n})_k \int_{B_k} \ln\left|\boldsymbol{x}-\boldsymbol{x}_0^{(m)}\right| \mathrm{d}s(\boldsymbol{x}) - \phi_k \fint_{B_k} \frac{\left(\boldsymbol{x}-\boldsymbol{x}_0^{(m)}\right)}{\left|\boldsymbol{x}-\boldsymbol{x}_0^{(m)}\right|^2}\cdot\boldsymbol{n}\,\mathrm{d}s(\boldsymbol{x})\right), \tag{3.7b}$$

for $m = 1, \ldots, N$, where $\phi_k = \phi(\boldsymbol{x}_0^{(k)})$, which are solved by Gaussian elimination. Logarithmic singularities at $\boldsymbol{x} = \boldsymbol{x}_0$ are dealt with in the usual fashion, namely an interval is taken around the singularity, within which the asymptotically expanded kernel is integrated analytically.

The non-smooth shape of the cantilever also requires special attention, as we expect singular behaviour in $|\boldsymbol{\sigma}\cdot\boldsymbol{n}|$ at the cantilever corners. We follow Loewenberg (1994*b*) and adjust the spacing of the boundary elements at the corners to account for $O(s^{-1/2})$ and $O(s^{-1/3})$ viscous and inviscid singularities, respectively, where s measures the distance from the corner. The contributions to the drag from the two-dimensional boundary layers wrapped around each corner are subdominant to terms in (3.6) (Loewenberg 1994*b*).

All sides of the square cantilever had 15 clustered boundary elements per half-length (or 10 for higher aspect ratios). For the values of γ considered here, decay of the unsteady flow away from the cantilever meant that wall integrals up to $|\boldsymbol{x}| = 10$ sufficed. Wall sub-intervals $[0, 2]$ and $[2, 10]$ were each partitioned into 25 uniformly spaced boundary elements, with the higher density of elements in $[0, 2]$ designed to capture the more rapidly varying wall stresses underneath the cantilever. Numerical convergence was verified by doubling the number of boundary elements on all surfaces and extending wall elements from 0 to 20. Numerical results are presented in § 5 below.

4. Asymptotic limits for a circular cantilever

Figure 2 charts the distinct asymptotic regions (I–VI) of (γ, Δ)-parameter space for a circular cantilever. In § 4.1 we treat the case where the distance that vorticity diffuses over one oscillation is much greater than the wall–cantilever separation ($\Delta \ll \gamma^{-1}$) and wall effects are controlled by viscosity. In § 4.2 the converse situation is investigated ($\Delta \gg \gamma^{-1}$), where inviscid wall interactions dominate. Finally § 4.3 describes the transition between these two states ($\Delta\gamma = O(1)$). In the following we denote the boundaries between regions (IV and V, say) as IV/V.

4.1. *Viscous wall interactions:* $\Delta \ll \gamma^{-1}$

4.1.1. *Small separations: region IV,* $\Delta \ll \min(1, \gamma^{-4/3})$

When the cantilever is close to the wall (region IV) we can model the flow in the gap between these two surfaces using lubrication theory, approximating the surface

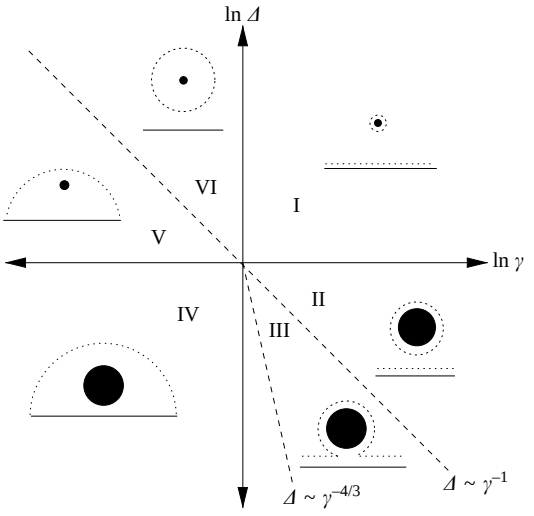

FIGURE 2. Asymptotic regions of (γ, Δ)-parameter space for a circular cantilever. A sketch inside each region shows the physical picture, with dotted lines indicating the distance over which vorticity diffuses during one oscillation.

of the cantilever with the parabola $y = \Delta + (x^2/2)$. Rescaling using

$$y = \Delta\,\check{y},\ x = \Delta^{1/2}\,\check{x},\ u = \Delta^{-1/2}\,\check{u},\ v = \check{v},\ p = \Delta^{-2}\,\check{p},\ \psi = \Delta^{-3/2}\,\check{\psi}, \tag{4.1}$$

the governing equations for the streamfunction become at leading order

$$\check{\psi}_{\check{y}\check{y}\check{y}} = \check{p}_{\check{x}}, \quad \check{p}_{\check{y}} = 0, \tag{4.2a}$$

$$\check{\psi}_{\check{x}}(\check{x}, 0) = 0, \quad \check{\psi}_{\check{y}}(\check{x}, 0) = 0, \quad \check{\psi}_{\check{x}}(\check{x}, 1 + \check{x}^2/2) = -1, \quad \check{\psi}_{\check{y}}(\check{x}, 1 + \check{x}^2/2) = 0, \tag{4.2b}$$

which yields

$$\check{\psi} = -\frac{2\check{x}\check{y}^3}{\left(1 + \frac{1}{2}\check{x}^2\right)^3} + \frac{3\check{x}\check{y}^2}{\left(1 + \frac{1}{2}\check{x}^2\right)^2}, \quad \check{p} = -\frac{24}{(2 + \check{x}^2)^2}, \tag{4.3}$$

so that

$$D = 3\sqrt{2}\pi\Delta^{-3/2} + O(\Delta^{-1/2}), \tag{4.4}$$

in agreement with Jeffrey & Onishi (1981). The flow outside the gap provides an $O(1)$ contribution to D when $\gamma \lesssim 1$. For $1 \ll \gamma \ll \Delta^{-3/4}$, the leading-order drag outside the lubrication region is $O(\gamma^2)$ but remains sub-dominant to (4.4). We discuss the case in which these contributions become comparable in § 4.3.2 below.

4.1.2. *Moderate separations: region IV/V, $\Delta = O(1)$, $\gamma \ll 1$*

When $\gamma \ll 1$ and $\Delta = O(1)$, (2.4*a*) reduces to the steady Stokes equations

$$\mathbf{0} = -\nabla p + \nabla^2 \boldsymbol{u}, \quad \nabla\cdot\boldsymbol{u} = 0, \tag{4.5}$$

subject to (2.4*b*). The steady Stokes problem of a circular cylinder translating perpendicularly to a horizontal wall was solved as a finite series in bipolar coordinates (3.1) by Jeffrey & Onishi (1981). A more compact form of the solution may be obtained using complex-variable techniques, such as adopted by Finn & Cox (2001), who determined the quasi-steady flow generated by one circular cylinder translating inside another. From their closed-form solution, we take the limit in which the

radius of the outer cylinder tends to infinity and recover a solution which reveals the singularity structure of the flow:

$$\psi = \beta_1 \left(\frac{x}{2} \ln \frac{r_+}{r_-} - \frac{2cx(y+c)}{r_+} + \frac{2c^2 x}{r_+} \right) + \beta_2 \left(\frac{x}{2} \ln \frac{r_-}{r_+} + \frac{2cx(y-c)}{r_-} + \frac{2c^2 x}{r_-} \right), \quad (4.6)$$

where $r_+ = x^2 + (y+c)^2$, $r_- = x^2 + (y-c)^2$, c is given by (3.1c) and

$$\beta_1 = \frac{c + \Delta + 1}{c - \Delta - 1} \beta_2, \quad \beta_2 = (c - \Delta - 1) \left(2c + (1+\Delta) \ln \left(\frac{1 + \Delta - c}{1 + \Delta + c} \right) \right)^{-1}. \quad (4.7)$$

Defining

$$\boldsymbol{M} = \begin{pmatrix} 1 & 0 \\ 0 & -1 \end{pmatrix}, \quad (4.8)$$

(4.6) can be interpreted as a superposition of (i) two Stokeslets within the cylinder at $(0, c)$ of strengths $-\beta_1 \boldsymbol{j}$ and $\beta_2 \boldsymbol{j}$, (ii) two image Stokeslets at $(0, -c)$ of strengths $\beta_1 \boldsymbol{j}$ and $-\beta_2 \boldsymbol{j}$, (iii) a stresslet at $(0, -c)$ of strength $-c\beta_1 \boldsymbol{M}$, (iv) a stresslet at $(0, c)$ of strength $c\beta_2 \boldsymbol{M}$ and (v) dipoles at $(0, -c)$ and $(0, c)$ of strengths $c^2 \beta_1 \boldsymbol{j}$ and $c^2 \beta_2 \boldsymbol{j}$ respectively. This description of the flow in terms of these singularities immediately gives the leading-order drag on the body to be

$$D = (\beta_2 - \beta_1) = -8\pi(1+\Delta) \left(2c + (1+\Delta) \ln \left(\frac{1 + \Delta - c}{1 + \Delta + c} \right) \right)^{-1}, \quad (4.9)$$

which is the net strength of the Stokeslets inside the cantilever. For $\Delta \ll 1$, (4.9) reduces to (4.4). It is instructive to obtain the large-Δ limit of (4.9) using an independent argument, as follows.

4.1.3. *Large separations: region V,* $1 \ll \Delta \ll \gamma^{-1}$

Even though in region V the wall–cantilever separation distance is large, the cantilever oscillates so slowly that vorticity diffuses a distance much greater than the distance to the wall during an oscillation. Thus we expect the cantilever to generate an $O(\ln \Delta)$ flow at the wall. An image flow of similar magnitude must be present to allow the boundary conditions at the wall to be satisfied. This is determined as follows. Setting $\boldsymbol{x} = \Delta \check{\boldsymbol{x}}$, $p = \Delta^{-1} \check{p}$, $\psi = \Delta \check{\psi}$ and $D = \Delta^{-1} \check{D}$ gives the following form for (2.4a):

$$-\check{\nabla} \check{p} + \check{\nabla}^2 \boldsymbol{u} = O((\Delta\gamma)^2), \quad \check{\nabla} \cdot \boldsymbol{u} = 0. \quad (4.10)$$

Since $\Delta\gamma \ll 1$ in region V, we have a quasi-steady flow at leading order. Suppose a point force is located at $\check{\boldsymbol{x}} = (0, 1)$ of unknown strength $4\pi A$, orientated perpendicular to the wall, on which no slip and no penetration are satisfied. Liron & Blake (1981) give the streamfunction for the resulting flow as

$$\check{\psi} = A \left(\check{x} \ln \sqrt{\frac{\check{x}^2 + (\check{y}-1)^2}{\check{x}^2 + (\check{y}+1)^2}} + \frac{2\check{x}(\check{y}+1)}{\check{x}^2 + (\check{y}+1)^2} - \frac{2\check{x}}{\check{x}^2 + (\check{y}+1)^2} \right). \quad (4.11)$$

We can identify the singularity structure of (4.11) as comprising Stokeslets of non-dimensional strength $4\pi A \boldsymbol{j}$ at $(0, 1)$ and $(0, -1)$, a dipole of strength $-4\pi A \boldsymbol{j}$ at $(0, -1)$ and a stresslet of strength $4\pi A \boldsymbol{M}$ at $(0, -1)$. We now modify (4.11) to produce a flow that satisfies no slip and no penetration at the cantilever's surface. The flow near the cylinder is assumed to be a superposition of a Stokeslet, uniform flow and dipole of

the form

$$\psi = Bx \ln \sqrt{x^2 + (y - 1 - \Delta)^2} + Cx + Ex/(x^2 + (y - 1 - \Delta)^2); \tag{4.12}$$

the boundary conditions on the cantilever surface are satisfied by choosing $C = -1 - B/2$ and $E = B/2$. Using the requirement that the outer flow (4.11) evaluated near the cylinder matches the inner flow (4.12) evaluated far from the cylinder, it can be shown (by intermediate matching) that

$$B = (\ln \Delta)^{-1} + (\ln \Delta)^{-2}(1 - \ln 2) + O((\ln \Delta)^{-3}), \quad A = \Delta B. \tag{4.13}$$

Thus the drag is given by the strength of the Stokeslet inside the cantilever

$$D = \frac{4\pi}{\ln \Delta} + \frac{4\pi(1 - \ln 2)}{(\ln \Delta)^2} + O\left(\frac{1}{(\ln \Delta)^3}\right), \tag{4.14}$$

in agreement with (4.9) for $\Delta \gg 1$. We shall exploit this constructive method again in § 4.3.1 below.

4.2. *Inviscid wall interactions: $\Delta \gg \gamma^{-1}$*

4.2.1. *Large separations: regions VI and I, $\Delta \gg \max(1, \gamma^{-1})$*

On the region VI/I boundary ($\Delta \gg 1$, $\gamma = O(1)$) the flow is largely inviscid. The flow must satisfy no penetration at the wall and (far from the cantilever) can be described by a dipole at the centre of the cantilever together with its image dipole in the wall. The flow produced by the image dipole is very weak at the cantilever, with velocity of order Δ^{-2}, and so the drag is approximately that exerted on an oscillating cylinder in unbounded fluid (Stokes 1851):

$$D = \pi \mathrm{i} \gamma^2 \left(1 + \frac{4K_1(\sqrt{\mathrm{i}}\gamma)}{\sqrt{\mathrm{i}}\gamma K_0(\sqrt{\mathrm{i}}\gamma)}\right) \tag{4.15}$$

subject to an $O(\Delta^{-1}\gamma^2)$ error, due to the generation of a cantilever surface pressure of this size from the image dipole (see Appendix C for the effect of slip on this drag result).

Taking the limit $\gamma \ll 1$ in (4.15), we obtain the drag in region VI ($\gamma \ll 1$):

$$D = -\frac{4\pi}{\ln \gamma} + \frac{4\pi c_0}{(\ln \gamma)^2} - \frac{4\pi c_0^2}{(\ln \gamma)^3} + \frac{4\pi c_0^3}{(\ln \gamma)^4} + O\left(\frac{1}{(\ln \gamma)^5}\right), \quad c_0 = \left(\frac{\mathrm{i}\pi}{4} + \epsilon_0 - \ln 2\right), \tag{4.16}$$

where $\epsilon_0 \approx 0.57721$ is Euler's constant. When $\gamma \gg 1$, (4.15) gives the leading-order drag in region I:

$$D = \pi \mathrm{i} \gamma^2 + 4\pi \sqrt{\mathrm{i}}\gamma + 3\pi + O(\gamma^{-1}), \tag{4.17}$$

provided that $\Delta \gg \gamma$. When this is the case, the wall–cantilever interaction does not feature in the $O(\gamma)$ secondary flow and so the drag is successfully approximated by that exerted on a circular cantilever oscillating in an unbounded fluid. However, if $\Delta \ll \gamma$ then the secondary $O(\gamma)$ flow is described by a collection of inviscid singularities located at the centre of the cantilever, together with their images in the wall. Rather than determine these directly, we use the Fourier-series method outlined below.

4.2.2. *Moderate and small separations: regions I and II, $\gamma \gg \max(1, \Delta^{-1})$*

On the region I/II boundary ($\Delta = O(1)$, $\gamma \gg 1$) we write

$$p = \gamma^2 p^{(0)} + \gamma p^{(1)} + \cdots, \quad \boldsymbol{u} = \boldsymbol{u}^{(0)} + \gamma^{-1}\boldsymbol{u}^{(1)} + \cdots, \tag{4.18}$$

and (2.4a) implies that

$$\mathrm{i}\boldsymbol{u}^{(0)} = -\nabla p^{(0)}, \quad \mathrm{i}\boldsymbol{u}^{(1)} = -\nabla p^{(1)}, \tag{4.19a, b}$$

where $\boldsymbol{u}^{(0)}(x,0) = \boldsymbol{0}$ and $\boldsymbol{u}^{(0)}|_S = \boldsymbol{j}$. Thus the primary and secondary flows are both inviscid with viscous effects restricted to thin boundary layers on the solid surfaces. Furthermore, the boundary layers that match to $\boldsymbol{u}_0$ determine the boundary conditions for $\boldsymbol{u}^{(1)}$. The secondary inviscid flow provides an $O(\gamma)$ drag contribution, commensurate with that from the boundary layers, which requires its retention.

A Fourier-series solution for the leading-order inviscid flow may be found by mapping the infinite Cartesian flow domain into a finite rectangular domain using bipolar coordinates (3.1) (see Appendix A), giving

$$\psi^{(0)} = 2c\sum_{n=1}^{\infty} e_n \sinh(n\eta)\sin(n\xi), \quad e_n = \frac{\mathrm{e}^{-n\eta_1}}{\sinh(n\eta_1)}, \tag{4.20}$$

where $\eta_1 = \cosh^{-1}(1+\Delta)$, from which we determine the slip velocities u_c^s on the cantilever and u_w^s on the wall. Using (4.19a) and (4.20) it is straightforward to show that the pressure is given by

$$p^{(0)} = 2\mathrm{i}c\sum_{n=1}^{\infty} e_n \cosh(n\eta)\cos(n\xi), \tag{4.21}$$

from which the leading-order $O(\gamma^2)$ drag may be determined.

Writing $y = \gamma^{-1}\tilde{y}$, we find the usual Stokes boundary layer on the wall in the form

$$u(x,\tilde{y}) = u_w^s(x)(1-\mathrm{e}^{-\sqrt{\mathrm{i}}\tilde{y}}) + O(\gamma^{-1}). \tag{4.22}$$

By transforming into polar coordinates with origin at the cantilever centre ($x = r\cos\theta$, $y = 1+\Delta+r\sin\theta$), and rescaling radial distances $r = 1+\gamma^{-1}\tilde{r}$, we find a Stokes boundary layer on the cantilever surface

$$u_\theta(\tilde{r},\theta) = u_c^s(\theta) - \left(u_c^s(\theta) - \cos\theta\right)\mathrm{e}^{-\sqrt{\mathrm{i}}\tilde{r}} + O(\gamma^{-1}), \tag{4.23}$$

where u_θ is the azimuthal component of velocity. The normal boundary-layer velocities drive the secondary $O(\gamma)$ inviscid outer flow, imposing upon it the following boundary conditions:

$$\psi^{(1)}(1,\theta) = \mathrm{i}^{-1/2}\left(-\cos\theta + u_c^s(\theta)\right), \quad \psi^{(1)}(x,0) = -\mathrm{i}^{-1/2}u_w^s(x), \tag{4.24}$$

which correspond to conditions at $\eta = 0$ and $\eta = \eta_1$ in bipolar space.

By expressing the boundary conditions (4.24) as a Fourier sine series in bipolar coordinates (see Appendix A), we can write the secondary inviscid flow as

$$\psi^{(1)} = \sum_{n=1}^{\infty}(a_n\cosh n\eta + b_n\sinh n\eta)\sin n\xi, \tag{4.25}$$

where

$$a_n = \frac{1}{\sqrt{\mathrm{i}}}[(n-1)e_{n-1} + (n+1)e_{n+1} - 2ne_n], \tag{4.26a}$$

$$b_n = \frac{1}{\sqrt{\mathrm{i}}}[2(n\,d_n + c)\,e_n - (d_n - c)(n-1)\,e_{n-1} - (d_n + c)(n+1)\,e_{n+1}], \tag{4.26b}$$

with $d_n = (2+\Delta)/\tanh n\eta_1$. The secondary pressure is then

$$p^{(1)} = \mathrm{i}\sum_{n=1}^{\infty}(a_n \sinh n\eta + b_n \cosh n\eta)\cos n\xi, \tag{4.27}$$

which, when combined with (4.21) and (4.23) and converted to polar coordinates, gives the drag

$$D = -\gamma^2\int_0^{2\pi} p^{(0)}(\theta)\sin\theta\,\mathrm{d}\theta - \gamma\int_0^{2\pi}\left(p^{(1)}(\theta)\sin\theta - \sqrt{\mathrm{i}}\left(u_c^s(\theta)-\cos\theta\right)\cos\theta\right)\mathrm{d}\theta, \tag{4.28}$$

where $p^{(0)}$, $p^{(1)}$ and u_c^s are given by (4.21), (4.27) and (A 4*a*), respectively. We show in § 5 below how (4.28) matches to (4.17) for sufficiently large Δ. The small-Δ limit of (4.28) is discussed in § 4.3.2 below.

4.3. *Viscous/inertial wall interactions: $\Delta\gamma = O(1)$*

We now consider situations in which the interaction between the particle and the wall is mediated by both viscous and unsteady inertial effects. This occurs primarily when the parameter $\tau \equiv \Delta\gamma = O(1)$.

4.3.1. *Large separations: region V/VI, $\Delta \sim \gamma^{-1} \gg 1$*

Between regions V and VI, the length scale for viscous diffusion is comparable to the separation between the cantilever and the wall. As in § 4.1.3, we find the flow by sequential construction, first introducing an oscillating two-dimensional Stokeslet (Avudainayagam & Geetha 1993), of unknown strength, combined with a dipole,

$$\psi = C\left(-\frac{1}{r}\left(1+\frac{2K_1(\sqrt{\mathrm{i}}\gamma)}{\sqrt{\mathrm{i}}\gamma K_0(\sqrt{\mathrm{i}}\gamma)}\right)+\frac{2K_1(\sqrt{\mathrm{i}}\gamma r)}{\sqrt{\mathrm{i}}\gamma K_0(\sqrt{\mathrm{i}}\gamma)}\right)\cos\theta, \tag{4.29}$$

where (r,θ) are polar coordinates centred on the cantilever. As these singular solutions induce non-zero flow at the wall, we must also add their image system (Chu & Kim 2001)

$$\psi_I = C\int_0^{\infty}\left[-A_1((k+q)\mathrm{e}^{-k(y+2\Delta)} - 2k\mathrm{e}^{-q(y+\Delta)-\Delta k}) - \frac{A_2}{\mathrm{i}\gamma^2}\left(\frac{k}{q}(k+q)\mathrm{e}^{-q(y+2\Delta)} - 2k\mathrm{e}^{-k(y+\Delta)-\Delta q}\right)\right]\frac{\sin kx}{(k-q)}\,\mathrm{d}k, \tag{4.30}$$

where $q=\sqrt{\mathrm{i}\gamma^2+k^2}$, $A_1 = 1 + 2K_1(\sqrt{\mathrm{i}}\gamma)/\sqrt{\mathrm{i}}\gamma K_0(\sqrt{\mathrm{i}}\gamma)$ and $A_2 = 2/K_0(\sqrt{\mathrm{i}}\gamma)$. At leading order, the image system generates a uniform flow near the cantilever, as can be seen by asymptotically evaluating the integral in (4.30) to give $\psi_I = Cx\Delta^{-2}I(\tau,\gamma) + O(\Delta^{-1})$, where

$$I(\tau,\gamma) = \int_0^{\infty}\left[-A_1\left(\frac{u(u+q_2)\,\mathrm{e}^{-2u}}{(u-q_2)}\right) - \frac{A_2}{\mathrm{i}\gamma^2}\frac{u^2(u+q_2)\,\mathrm{e}^{-2q_2}}{q_2\,(u-q_2)} + 2\left(A_1+\frac{A_2}{\mathrm{i}\gamma^2}\right)\frac{u^2\,\mathrm{e}^{-(u+q_2)}}{(u-q_2)}\right]\mathrm{d}u \tag{4.31}$$

and $q_2 = \sqrt{u^2+\tau^2}$. Consequently, the flow local to the cantilever is given by

$$\psi = C\left(-\frac{1}{r}\left(1+\frac{2K_1(\sqrt{\mathrm{i}}\gamma)}{\sqrt{\mathrm{i}}\gamma K_0(\sqrt{\mathrm{i}}\gamma)}\right)+\frac{2K_1(\sqrt{\mathrm{i}}\gamma r)}{\sqrt{\mathrm{i}}\gamma K_0(\sqrt{\mathrm{i}}\gamma)}+\frac{I(\tau,\gamma)r}{\Delta^2}\right)\cos\theta + O(\Delta^{-1}). \tag{4.32}$$

We can satisfy $\psi = -r\cos\theta$ on S by setting $C = \left(1 - \Delta^{-2} I(\tau, \gamma)\right)^{-1}$. Only the Stokeslet exerts drag on the cantilever and thus the drag is

$$D = \pi C \mathrm{i}\gamma^2 \left(1 + \frac{4K_1(\sqrt{\mathrm{i}}\gamma)}{\sqrt{\mathrm{i}}\gamma K_0(\sqrt{\mathrm{i}}\gamma)}\right) \approx \left(1 - \frac{I(\tau,\gamma)}{\Delta^2}\right)^{-1} \left(\frac{4\pi}{\ln 2 - \ln(\sqrt{\mathrm{i}}\gamma) - \epsilon_0} + O(\gamma^2)\right), \tag{4.33}$$

where, as in § 4.2.1, ϵ_0 is Euler's constant. In the limit $\tau \ll 1$ we are able to evaluate the integral $I(\tau, \gamma)$ asymptotically, to obtain

$$D = \frac{4\pi}{(\ln\Delta + \ln 2 - 1 - \tau^2/4)} + O(\gamma^2(\ln\Delta)^{-1}, (\Delta^2 \ln\gamma)^{-1}, \gamma^4), \tag{4.34}$$

with $\tau^2/4$ giving the first inertial correction to the quasi-steady result (4.14) for region V. Conversely, in the limit $\tau \gg 1$, since $I/\Delta^2 \propto (\tau^2 \ln\tau)^{-1}$ we see that (4.33) reduces to the region-VI limit (4.15).

4.3.2. *Small separations: region III, $\gamma^{-4/3} \lesssim \Delta \lesssim \gamma^{-1} \ll 1$*

A second interaction between viscous, inertial and wall effects occurs in region III. The boundaries of this region are defined as follows. For $\Delta \sim \gamma^{-1} \ll 1$ (the II/III boundary), the Stokes layers on the cantilever and wall are comparable in thickness to the wall–cantilever spacing. Thus the inner lubrication flow has a mixed viscous–inertial structure over a horizontal length scale $\Delta^{1/2}$. However, the drag remains dominated by the $O(\gamma^2)$ inviscid contribution from the outer flow. As Δ is reduced, the lubrication region develops a nested structure, with a viscous region of width $\Delta^{1/2}$ (contributing an $O(\Delta^{-3/2})$ drag, see (4.4)) lying within a viscous/inertial region of width $\gamma^{-1/2}$. Once $\Delta = O(\gamma^{-4/3})$, the drag from the viscous region becomes comparable with the leading-order inertial drag in the outer region; this defines the III/IV boundary. For $\Delta \ll \gamma^{-4/3}$, we enter region IV and (4.4) dominates.

We derive here an expression connecting the behaviour in regions II and IV. It is sufficient to work along the region II/III boundary, since the nested boundary layer structure in region III is captured implicitly. Along this boundary, we anticipate drag contributions at $O(\gamma^2)$ (inviscid outer), $O(\gamma^{3/2})$ (viscous/inviscid inner) and $O(\gamma)$ (viscous outer). Thus both inner and outer regions are needed for a reliable estimate of the drag.

The inviscid flow is found by conformally mapping the outer flow domain, in which the cantilever appears to be in contact with the wall, to an infinite strip, where Fourier transform methods yield the following streamfunction for the flow (see Appendix B):

$$\psi = 4\pi \int_0^\infty \left(\frac{\mathrm{e}^{-2\pi k}}{\sinh 2\pi k}\right) \sinh(2\pi k\eta) \sin(2\pi k\xi)\, \mathrm{d}k. \tag{4.35}$$

In the lubrication region, (4.1) yields the following governing equations:

$$\check{\psi}_{\check{y}\check{y}\check{y}} - \mathrm{i}\tau^2 \check{\psi}_{\check{y}} = \check{p}_{\check{x}}, \quad \check{p}_{\check{y}} = 0, \tag{4.36a}$$

up to an $O(\Delta)$ correction, subject to the boundary conditions (4.2*b*), which are satisfied by

$$\check{\psi} = A(\check{x})\mathrm{e}^{\sqrt{\mathrm{i}}\tau\check{y}} + B(\check{x})\mathrm{e}^{-\sqrt{\mathrm{i}}\tau\check{y}} + (\sqrt{\mathrm{i}}\tau)^{-2} C(\check{x})\check{y} + (\sqrt{\mathrm{i}}\tau)^{-2} E(\check{x}). \tag{4.37a}$$

Defining $\kappa = \sqrt{\mathrm{i}\tau}\,(1 + \check{x}^2/2)$, the coefficients in (4.37*a*) are

$$\left.\begin{aligned} A(\check{x}) &= \frac{1}{2}\left(\frac{\check{x}\,(1-\mathrm{e}^{-\kappa})}{\kappa\sinh\tau - 2\cosh\kappa + 2}\right), \quad B(\check{x}) = \frac{1}{2}\left(\frac{\check{x}\,(1-\mathrm{e}^{\kappa})}{\kappa\sinh\kappa - 2\cosh\kappa + 2}\right), \\ C(\check{x}) &= \frac{-(\sqrt{\mathrm{i}\tau})^3\,\check{x}\sinh\kappa}{\kappa\sinh\kappa - 2\cosh\kappa + 2}, \qquad E(\check{x}) = \frac{-(\sqrt{\mathrm{i}\tau})^2\,\check{x}(1-\cosh\kappa)}{\kappa\sinh\kappa - 2\cosh\kappa + 2}. \end{aligned}\right\} \tag{4.37b}$$

For $\tau \ll 1$ with $\check{x} = O(1)$, (4.37) reduces to (4.3).

The leading-order drag in both the inner and outer flows comes from the pressure, whose gradient we now express as a composite expansion. Adding the outer p_θ^O and inner p_θ^I expressions for the pressure gradient, and subtracting off their common expression p_θ^C in the intermediate region between inner and outer, we arrive at the following uniformly valid expression for the pressure gradient on S:

$$p_\theta = \Delta^{-2}\big(p_\theta^I + \tau^2 p_\theta^O - \tau^2 p_\theta^C\big), \tag{4.38a}$$

where

$$p_\theta^I = \Xi^3\Theta\sinh\alpha\,(\alpha\sinh\alpha - 2\cosh\alpha + 2)^{-1}, \quad \alpha = \Xi\left(1 + \Theta^2/2\right), \tag{4.38b}$$

$$p_\theta^O = 8\mathrm{i}\pi^2\int_0^\infty \left(\frac{k\mathrm{e}^{-2\pi k}}{\tanh 2\pi k}\right)\frac{\sin(2\pi k\cos\theta(1+\sin\theta)^{-1})}{(1+\sin\theta)}\,\mathrm{d}k, \tag{4.38c}$$

$$p_\theta^C = 2\mathrm{i}\,(\theta + \pi/2)^{-1}, \tag{4.38d}$$

$\Xi = \sqrt{\mathrm{i}\Delta\gamma}$ and $\Theta = \Delta^{-1/2}\,(\theta+\pi/2)$. We next numerically integrate p_θ for the pressure, which is then used to determine the drag:

$$D = 2\int_0^\pi \left(\int_0^\beta p_\theta\,\mathrm{d}\theta\right)\sin\beta\,\mathrm{d}\beta. \tag{4.38e}$$

We have not included the cantilever boundary layers and secondary inviscid flows in the outer flow, but (4.38) successfully connects the leading-order drag in region II with that in region IV, as demonstrated numerically in § 5.1.2 below.

5. Results

We now present numerical results for circular and rectangular cantilevers. In § 5.1 we compare calculations for circular cantilevers using the scheme outlined in § 3.1 with the asymptotic predictions developed in § 4 in limiting cases. For rectangular cantilevers (§ 5.2), using the scheme described in § 3.2, we investigate the effects of varying the aspect ratio and we compare the drag with that for circular cantilevers.

5.1. *Circular cantilevers*

5.1.1. *Streamlines*

Figure 3 shows two sets of streamlines for a circular cantilever at unit distance from the horizontal wall $y = 0$, each showing the instantaneous behaviour at three distinct times in the oscillation cycle for $\gamma^2 = 1$ (panels *a–c*) and $\gamma^2 = 10$ (panels *d–f*). At both frequencies we see that there is an up–down asymmetry in the streamlines induced by the presence of the wall. However, this asymmetry is less pronounced for $\gamma^2 = 10$, indicating that, as viscous effects become confined to boundary surfaces, wall effects diminish elsewhere in the flow. At $t = 0$ the cantilever passes through its zero-displacement position; as the cantilever changes direction at $t = \pi/2$, closed

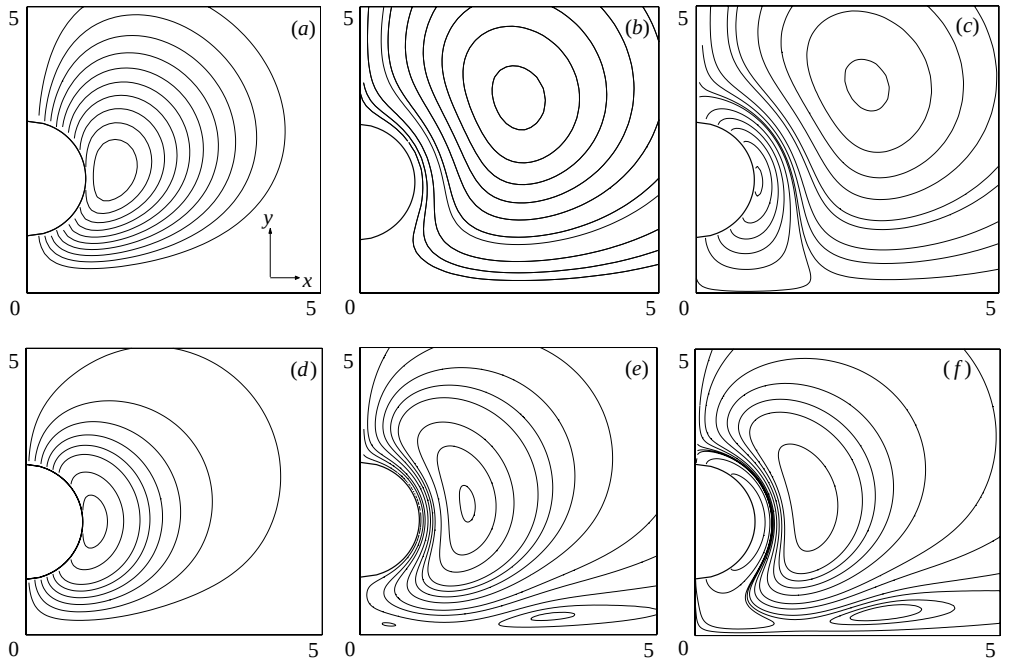

FIGURE 3. Streamlines for a circular cantilever when $\Delta = 1$ at (*a*) $t = 0$, (*b*) $t = \pi/2$, (*c*) $t = \pi/2 + 0.1$ when $\gamma^2 = 1$ and at the same times for $\gamma^2 = 10$, (*d*, *e* and *f* respectively). The wall is located along the x-axis.

streamlines are shed from the cantilever's surface. Such flow reversal has been noted in other studies of oscillating bodies (Pozrikidis 1989*b*; Loewenberg 1994*b*) in the absence of external boundaries. In the presence of a nearby wall we observe reversal on this external boundary which, at $\gamma^2 = 10$, occurs fractionally earlier than the reversal on the body's surface.

5.1.2. *Drag*

Figure 4 presents numerical drag computations for a circular cantilever alongside the corresponding asymptotic limits, highlighting the trends in drag as Δ and γ are varied. For fixed γ (figure 4*a*, *b*), a decrease in Δ produces a monotonic increase in the drag's modulus and a monotonic decrease in its phase. This change is seen to be a function of γ, occurring at lower values of Δ as γ is increased. The results for fixed Δ (figure 4*c*, *d*) show that the drag's modulus increases and becomes less sensitive to separation distance at larger γ. The phase tends towards the inviscid limit of $\pi/2$ as γ is increased, but with the rate of convergence slower at small Δ.

An important feature of these results is the comprehensive coverage of parameter space provided by the asymptotics, with good continuity between these limits. Thus we are able to make a circuit of parameter space and use the asymptotics to explain the dominant features which contribute to the drag. In figure 4(*a*, *b*) we see that, at sufficiently small separations, steady lubrication theory (region IV, (4.4)) approximates the drag well even at high frequencies. However, as the separation is increased the behaviour of the drag depends upon the frequency. At low frequencies the lubrication approximation to the drag is maintained until the separation increases to roughly one tenth of the cantilever radius, at which point the finite dimensions of the cantilever need to be taken into account. A geometrically more advanced quasi-steady estimate

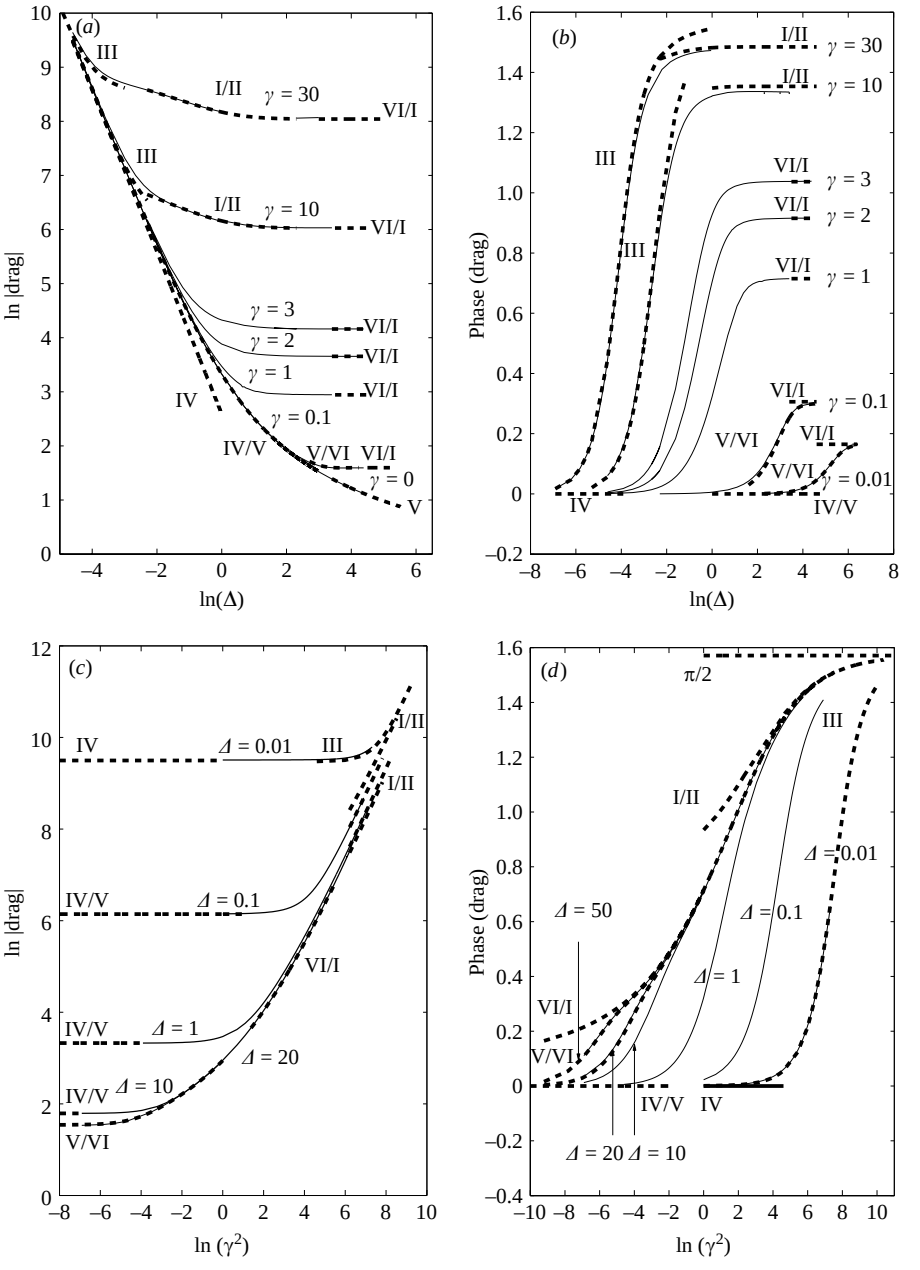

FIGURE 4. Modulus (*a*) and phase (*b*) of the drag when $\gamma^2 = 0, 0.1, 1, 2, 3, 10, 30$ plotted over a range of Δ, together with modulus (*c*) and phase (*d*) of the drag when $\Delta = 0.01, 0.1, 1, 10, 20$ and 50, plotted over a range of γ. Thin solid lines correspond to numerical computations, whilst asymptotic results for regions I/II (4.28), III (4.38*e*), IV (4.4), IV/V (4.9), V (4.14), V/VI (4.33) and VI/I (4.15) (covering both I and VI) are shown with thicker dashed lines.

when $\Delta = O(1)$ (IV/V, (4.9)) and the steady Stokeslet image system, valid for $\Delta \gg 1$ (V, (4.14)), work well until the separation becomes comparable with the viscous length γ^{-1}, at which point it breaks down due to the importance of unsteadiness on these length scales. However, here we are able to turn to the unsteady Stokeslet image

system (V/VI, (4.33)) which provides accurate estimates for the drag right up to the unsteady unbounded limit (VI/I, (4.15)). Conversely, at high frequencies, steady lubrication theory quickly fails and we require the merged boundary-layer model to describe the transition to inertia-dominated flow (III, (4.38*e*)). This takes us to the limit of inviscid flow, with viscous effects restricted to thin boundary layers on the solid surfaces (I/II, (4.28)). In this limit, even at $O(1)$ separations the presence of the wall is seen to exert little influence upon the drag, illustrating the weaker nature of the inviscid wall interactions in the high-frequency regime.

An alternative perspective is offered by figure 4(c, d), which shows how the modulus and phase of the drag both increase monotonically with frequency at fixed separation. At sufficiently large frequencies an inviscid flow plus boundary layers (I/II) provides a good drag estimate, capturing the increase in the drag's modulus at small separations due to the inviscid wall interaction. However, in the small separation limit, as the frequency is reduced, the boundary-layer model rapidly fails and the merged boundary-layer model (III) describes the transition to quasi-steady lubrication flow (IV). At large separations the boundary-layer approximation persists for longer, yet provides a drag which is already estimated well by the unbounded fluid limit (VI/I). As the frequency is decreased still further the distance over which vorticity diffuses grows until becoming comparable with the large wall–cantilever separation, resulting initially in a wall interaction which is governed by unsteady viscous flow and finally in an interaction governed by steady viscous flow; the unsteady Stokeslet image system (V/VI) is seen to capture this transition.

5.2. *Rectangular cantilevers*

We now examine the effect of geometry upon drag using boundary-element results for rectangular cantilevers. Calculating streamlines is arduous with boundary-element methods; however, surface stresses are readily obtainable and serve to illustrate the impact of the nearby wall. Figure 5 shows the vertical component of the surface stress on the wall and cantilever, with square cross-section, for the case $\gamma = \Delta = 1$. The difference in stress profiles on the top and bottom of the cantilever, as well as the skewed shear stress on the cantilever's side, are both attributable to the wall. The integrable stress singularities at each corner of the body are evident, although in practice it is likely that geometrical smoothing or wall slip (particular in gases) would act to regularize this singular behaviour.

5.2.1. *Drag*

Rectangular cantilever drag results are presented in figure 6 for two cantilever cross-sections: thin (aspect ratio 20) and square. The dependence of modulus and phase on Δ and γ is broadly similar to the circular case; however, we are now in a position to assess the impact of differing aspect ratio. The dash–dotted lines represent a lubrication limit for the drag on the cantilever, which is calculated analogously to the $\Delta \ll 1$ case with a circular cantilever, but with the rescalings

$$y = \Delta \check{y},\ x = \check{x},\ u = \Delta^{-1}\check{u},\ v = \check{v},\ p = \Delta^{-3}\check{p},\ D = \Delta^{-3}\check{D}. \tag{5.1}$$

An analysis similar to that in § 4.3.2 gives a lubrication drag of

$$D = \frac{2}{3}\mathrm{i}\Delta^{-1}\gamma^2 \left(\frac{\sqrt{\mathrm{i}}\tau \sinh \sqrt{\mathrm{i}}\tau}{2 - 2\cosh \sqrt{\mathrm{i}}\tau + \sqrt{\mathrm{i}}\tau \sinh \sqrt{\mathrm{i}}\tau} \right), \quad \tau = \gamma\Delta \tag{5.2}$$

plus an $O(\gamma^2)$ correction due to flow outside the gap. The impact on this drag of introducing slip is examined in Appendix C.

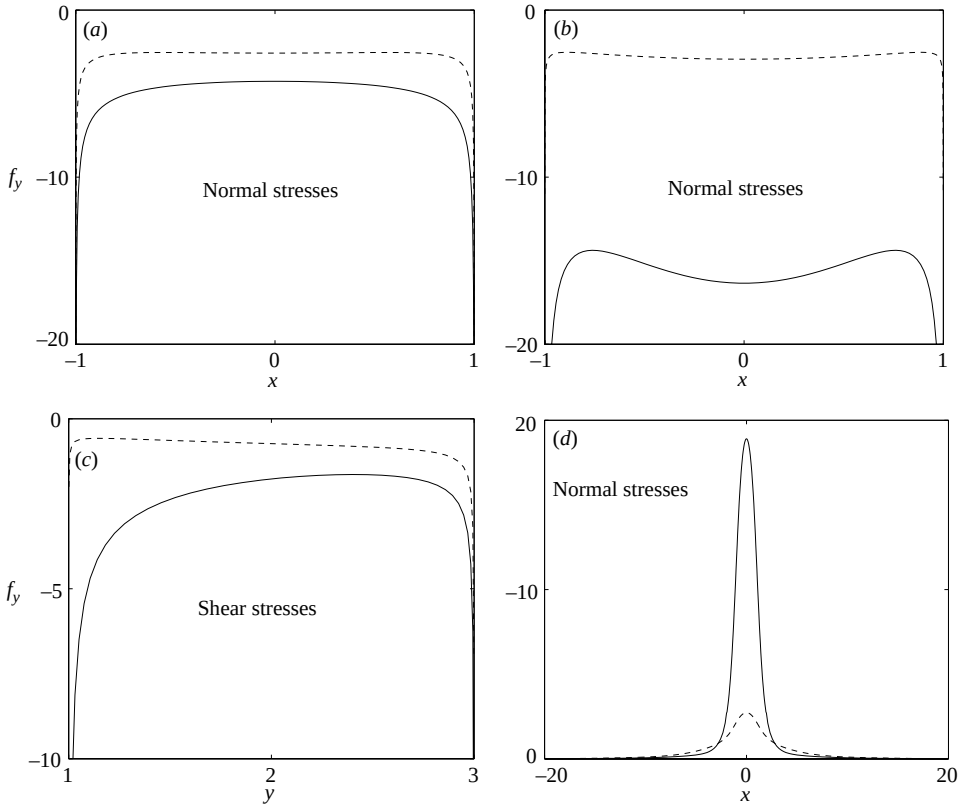

FIGURE 5. y-component of surface stress on (a) the top, (b) bottom and (c) side of a rectangular cantilever with unit aspect ratio, when $\gamma = 1$ and $\Delta = 1$. Plot (d) shows the normal y-component of surface stress on the wall. Real parts are given by a solid line and imaginary parts by a dashed line.

In the quasi-steady limit, $\tau \to 0$, (5.2) reduces to $D = 8\Delta^{-3}$, in agreement with Kim *et al.* (2001), who also calculate the first drag correction arising from a quasi-steady outer flow when the rectangle is infinitely thin. Asymptotically matching the lubrication flow to a local flow at the cantilever's edges and to an outer flow where the presence of the plate is accounted for by point sources on the wall, they obtained

$$D = 8\Delta^{-3} + 14.8560\Delta^{-2}. \tag{5.3}$$

Figure 6(a, c) illustrates how this correction improves the drag estimate. Moreover, figure 6(c, d) demonstrates the effectiveness of (5.2) in capturing the influence of flow inertia on the drag in the lubrication regime, as well as the effectiveness of the inviscid boundary-element-method predictions (3.6) at high frequencies.

These results confirm that thin cantilevers experience less drag than square ones, but this distinction is diminished when quasi-steady flow dominates the drag, i.e. when either γ or Δ become sufficiently small. If the cantilever is sufficiently close to the wall, the phase of the drag is independent of the cantilever aspect ratio. However, as the separation is increased the phases in each case differ, particularly at higher frequencies. If the separation is increased still further, the phase appears, once again, to become less sensitive to the thickness of the cantilever.

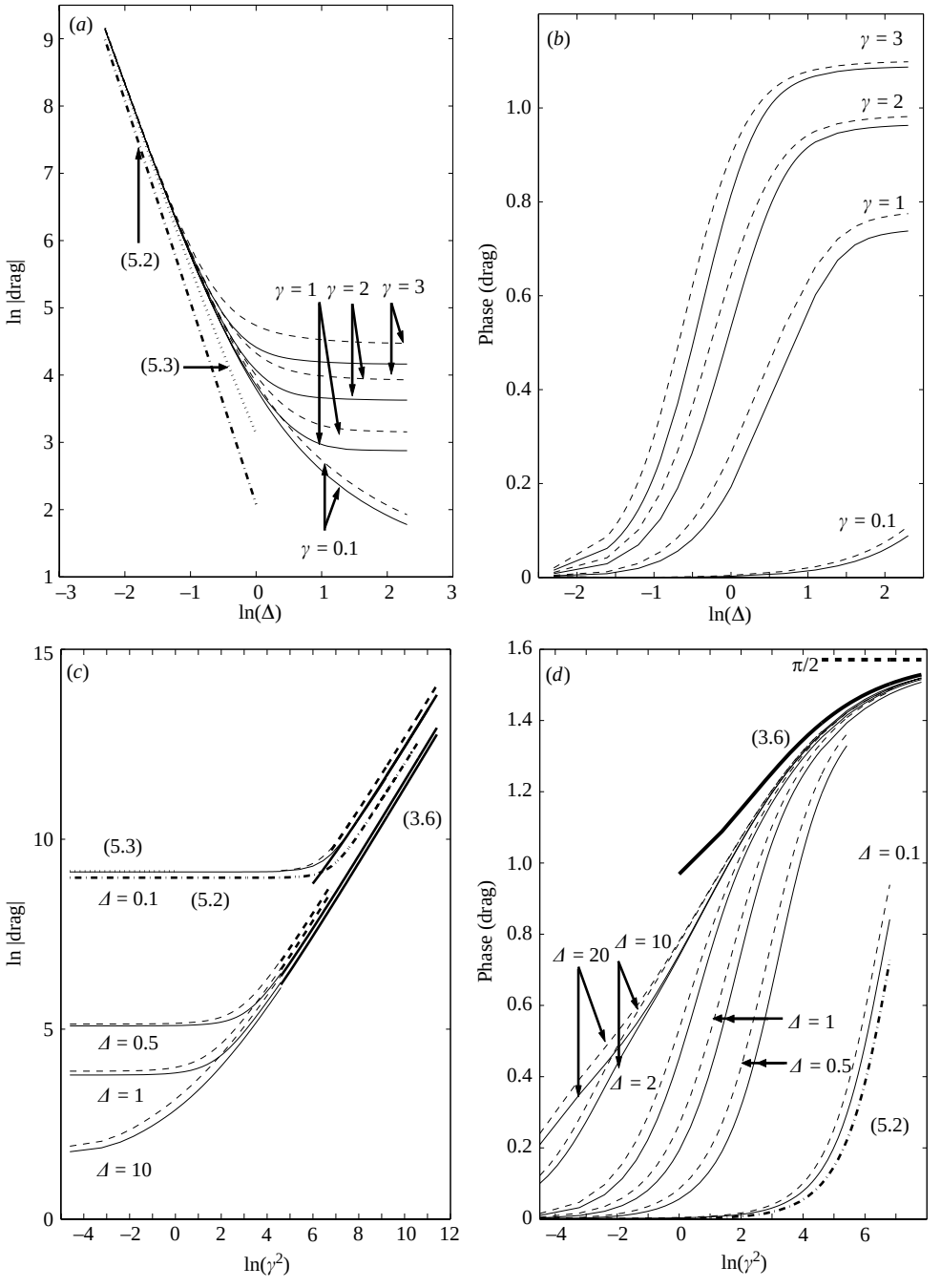

FIGURE 6. Modulus (*a*) and phase (*b*) of the drag on a cantilever, of width 2 and thickness 0.1 (solid line) or 2 (dashed line), over a range of Δ and the modulus (*c*) and phase (*d*) of the drag over a range of γ. The unsteady lubrication limit (5.2), for an infinitely thin plate, is marked by a thick dash–dotted line, and is plotted alongside a quasi-steady limit which accounts for the full geometry (5.3). The thick solid lines in (*c*, *d*) show drag predictions computed using a separate boundary-element scheme for the potential flow (3.6).

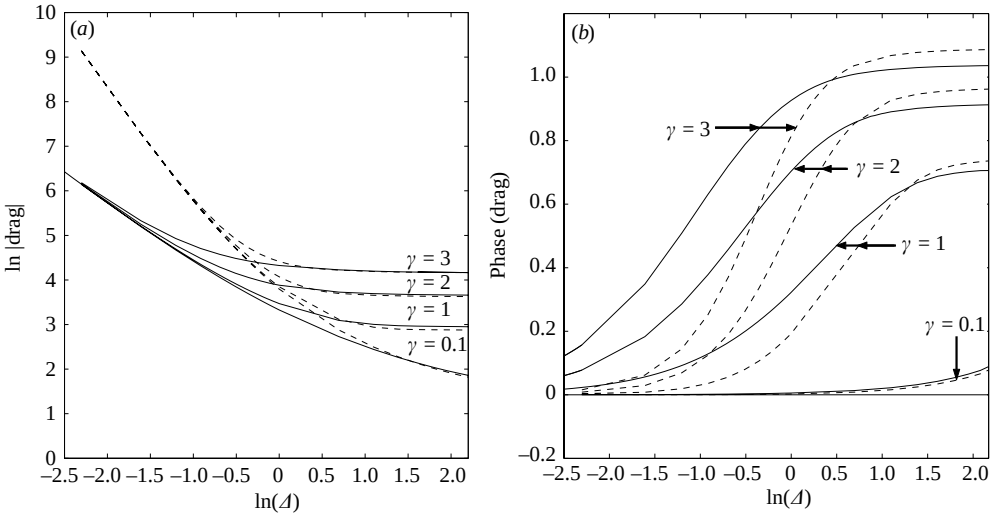

FIGURE 7. Comparison between (*a*) the modulus and (*b*) the phase of the drag on a circular cantilever (solid line) and rectangular cantilever with thickness 0.1 (dashed line).

Comparing circular and rectangular cantilevers (figure 7) we see that the drag on a thin rectangular cantilever is similar to that on a circular cantilever of the same width for sufficiently large wall–cantilever separations. The similarity between the drag for an oscillating infinitely thin plate and an oscillating cylinder in an unbounded fluid, first noted by Tuck (1964), persists at moderate distances from a rigid wall (and moreover, as shown in figure 6(*a*), extends to cantilevers of other aspect ratios at low frequencies). However, the drag on a thin cantilever diverges significantly from that on a circular cantilever as Δ falls. For separations less than roughly one cantilever width there is a dramatic increase in the drag's modulus and a significant drop in its phase (the former more so and the latter less so at low frequencies; see figure 7*a*, *b*), reflecting the differing size of the lubrication regions in each case.

6. Summary and conclusions

We have examined the influence of a nearby rigid wall on the drag experienced by a two-dimensional oscillating cantilever as a function of the dimensionless oscillation frequency γ^2, the separation distance Δ and the cantilever shape. Drag predictions have been obtained numerically, using a finite-difference method (for circular cantilevers) and a boundary-element method (for rectangular cantilevers), accompanied (for circular cantilevers) by extensive asymptotic results spanning all extremes of (γ, Δ)-parameter space. We assumed throughout that oscillation amplitudes were small enough for the linearized Stokes equations and linearized boundary conditions to be valid. A summary of our leading-order asymptotic drag expressions for circular cylinders (in dimensional form) has been compiled in table 1.

Our results demonstrate the boundaries in parameter space across which wall effects have a significant leading-order influence on the drag. At low frequencies ($\gamma \ll 1$), wall effects are important for $\Delta = O(\gamma^{-1})$, indicating that wall interactions are significant even at large separation distances (as expected from Stokes' paradox). As Δ is reduced from an initially large value, we demonstrated how wall effects have their first non trivial impact when $\Delta \sim \gamma^{-1}$ by using the image system of an unsteady Stokeslet to

Region	D^*
IV	$3\sqrt{2}\pi\mu U\,\Delta^{-3/2}$
IV/V	$-8\pi\mu U(1+\Delta)\left(2\sqrt{\Delta(\Delta+2)}+(1+\Delta)\ln\left(\frac{1+\Delta-\sqrt{\Delta(\Delta+2)}}{1+\Delta+\sqrt{\Delta(\Delta+2)}}\right)\right)^{-1}$
V	$\frac{4\pi\mu\, U}{\ln\Delta}+\frac{4\pi\mu\, U\,(1-\ln 2)}{(\ln\Delta)^2}$
V/VI	$\mu\, U\left(1-\frac{I(\Delta,\, R\sqrt{\omega\rho/\mu})}{\Delta^2}\right)^{-1}\left(\frac{4\pi}{\ln 2-\ln(R\sqrt{\mathrm{i}\omega\rho/\mu})-\epsilon_0}\right)$
VI	$-\frac{4\pi\mu U}{\ln R\sqrt{\omega\rho/\mu}}+\frac{4\pi\,(i\pi/4+\epsilon_0-\ln 2)\,\mu U}{(\ln R\sqrt{\omega\rho/\mu})^2}$
VI/I	$\frac{\mathrm{i}\pi R^2\omega\rho\, U}{\mu}\left(1+\frac{4K_1(R\sqrt{\mathrm{i}\omega\rho/\mu})}{R\sqrt{\mathrm{i}\omega\rho/\mu}K_0(R\sqrt{\mathrm{i}\omega\rho/\mu})}\right)$
I	$\mathrm{i}\pi R^2\omega\rho U/\mu+4\pi U R\sqrt{\mathrm{i}\omega\rho/\mu}$
I/II	See (4.28)
III	See (4.38*e*)

TABLE 1. Summary of the leading-order drag $\mathrm{Re}(D^*\,\mathrm{e}^{\mathrm{i}\omega t})$ experienced by a circular cylinder of radius R oscillating in a fluid of viscosity μ with frequency ω normally to a wall, with its centre a height y_0 above the wall. Here $\Delta=(y_0-R)/R$, $\epsilon_0\approx 0.57721$ and I is given by (4.31). Regions of parameter space are as shown in figure 2.

determine the drag on a circular cylinder. This image system is distributed along the wall, thus appearing as an integral in the expression for the drag (4.33). For $\Delta=o(\gamma^{-1})$ the flow is dominated by quasi-steady viscous effects: the magnitude of the drag rises rapidly (figures 4*a*, *b*, 6*a*, *b*) until being dominated by viscous lubrication forces as $\Delta\to 0$. In this lubrication regime there is, as expected, a substantial difference between circular and rectangular cantilevers (figure 7*a*) because of the different aspect ratios of the thin-gap regions. At high frequencies ($\gamma\gg 1$), when viscous effects are typically confined to thin Stokes layers, the wall has negligible effect on the drag until the separation is very small. For circular cantilevers, for $\Delta\sim\gamma^{-1}$, there is the first non-trivial change in the structure of the flow when the Stokes layers on the cantilever and wall overlap. However it is not until $\Delta\sim\gamma^{-4/3}$ that the leading-order drag depends explicitly on Δ. For sufficiently small Δ, the quasi-steady lubrication drag dominates that from the outer oscillatory flow. For rectangular cantilevers oscillating at high frequency the wall has a much more substantial effect. For $\gamma^{-1}\ll\Delta\ll 1$ the unsteady acceleration of liquid along the narrow gap dominates the drag (see (5.2); this is an inviscid lubrication regime), for $\Delta\sim\gamma^{-1}$ the Stokes layers fill the gap, and then for $\Delta\ll\gamma^{-1}$ the dominant drag is from viscous lubrication forces.

One of the most striking findings for rectangular cantilevers is the very weak dependence of drag on aspect ratio. Comparing rectangular cantilevers with aspect ratios of 1 and 20, figure 6 shows (not surprisingly) negligible difference in the thin-gap limit ($\Delta\ll 1$), and differences of only a few percent at high frequencies. This high-frequency insensitivity is also demonstrated in figure 7, which reflects Tuck's (1964) observation that a plate serves as a good model for a cylinder (in the absence of a wall). However, figure 7 provides clear evidence of the limitations of (4.15), an

approximation used commonly in AFM studies (e.g. Sader 1998): the drag on a thin rectangular cantilever rises dramatically (note the logarithmic scale in figure 7) and the phase falls substantially as Δ falls below $O(1)$ values, an experimentally realized regime.

We have assumed throughout that the amplitude of oscillation is small enough for nonlinear effects such as steady streaming to be negligible. We implicitly assumed the oscillation amplitude to be much smaller than the boundary-layer thickness, which is a restrictive condition at high frequencies. Furthermore, we have also taken no account of possible flow instabilities. However, in a regime in which the AFM operates (with the cantilever close to the sample but oscillating at very high frequency, with $\gamma^{-1} \ll \Delta \ll 1$), the flow is likely to exhibit some interesting weakly nonlinear effects. Suppose a rectangular cantilever oscillates with amplitude εR, where R is the cantilever width. The $O(\varepsilon^2)$ steady-streaming flow beneath the cantilever is likely to resemble that in an infinitely long pulsating channel, as described by Secomb (1978). Subsequently Hall & Papegeorgiou (1999) showed how a nonlinear flow synchronous with the oscillating wall arises for (in our variables) $\gamma > 3.39/\varepsilon$ (this is a large-Reynolds-number asymptotic limit, assuming $\gamma^2\Delta^2 \gg 1$; a similar result was also obtained by Watson *et al.* 1990), and that this flow then loses stability to quasi-periodic oscillations for $\gamma > 5.99/\varepsilon$. This indicates that, even at small amplitudes, an AFM cantilever can experience a steady force (due to steady streaming) as well as a force that fluctuates at a frequency different to that of the driver. At lower Reynolds numbers, the quasi-steady flow between pulsating plates may also be unstable to growing Tollmien–Schlichting waves (Stuart *et al.* 1990).

A key aspect of any experimental system is three-dimensionality, and we should be concerned that our assumption of two-dimensional flow may be unrealistic. Certainly complex cantilever shapes, or tilt relative to the plane, will generate three-dimensional flows. For simplicity, let us consider instead a circular cylinder of length $\Lambda \gg 1$ (measured relative to its radius R) oscillating with its axis parallel to the wall, again at small amplitudes in a direction normal to the wall. Two effects promote two-dimensionality. First, when the cylinder is close to the wall and the flow is quasi-steady, the wall screens the flow from end effects; this will be the case for $\Delta \ll \Lambda$ and the frequency sufficiently low. Second, when the cylinder is oscillating at sufficiently high frequency, the limited distance over which vorticity diffuses from the cylinder surface during one period makes the viscous component of the flow around the cylinder predominantly two-dimensional provided $\gamma \gg 1/\Lambda$ (so that the majority of the viscous flow around the cylinder does not 'feel' the finite length of the cylinder); we have already seen that the outer inertial flow (in regions VI and I) is then largely insensitive to the wall, since wall–body interactions in two dimensions occur via relatively weak image dipoles. As the body moves away from the wall, across $\Delta \sim \Lambda$ with $\gamma \gg 1/\Lambda$, the inviscid flow may develop a three-dimensional structure but the drag will almost certainly remain largely insensitive to Δ. Thus we anticipate that the drag will show leading-order dependence on the finite length of the cylinder only for $\gamma \lesssim 1/\Lambda$, $\Delta \gtrsim \Lambda$ (in our present formulation, this represents very slow oscillations of a long body very far from the wall). We present calculations in this regime using slender-body theory for unsteady Stokes flow elsewhere (Clarke *et al.* 2005). The argument above supports the application of the present two-dimensional model to experiments involving oscillating cantilevers with simple geometric shapes.

Within the AFM community there is considerable interest in quantifying and exploiting hydrodynamic effects both for tapping mode (probing sample properties) and thermal calibration. As previously mentioned, the determination

	Width (R) (cm)	Thickness ($2W$) (cm)	Visc. (ν) (cm^2s^{-1})	Sep. ($y_0 - h$) (cm)	Freq. (ω) Hz	Δ	γ^2
Tapping-mode	10^{-3}	10^{-4}	10^{-2}	10^{-4}	10^4–10^5	0.1	1–10
Calibration	10^{-3}	10^{-4}	10^{-2}	10^{-2}	10^3–10^4	10	0.1–1

TABLE 2. Typical operating parameters for AFM imaging and calibration (Santos & Castanho 2004; Chon *et al.* 2000).

of cantilever spring constants presents a major challenge, with one widely used non-intrusive (and often imprecise) technique involving the analysis of thermal spectra (Sader 1998; Paul & Cross 2004). Currently thermal calibration takes place in essentially unbounded fluid. However, the hydrodynamic results presented here, when incorporated into a model of cantilever dynamics, offer the means to quantify the spectral flattening reported by Benmouna & Johannsmann (2002) and Nnebe & Schneider (2004) and, consequently, opens up new opportunities to extract quantities such as the cantilever spring constant more precisely. Representative parameter values for AFM imaging and calibration are given in table 2.

As mentioned in § 1, the microscopic dimensions of AFM cantilevers raise important questions about the validity of both the no-slip condition and the continuum approximation. The effects of slip are illustrated in Appendix C. In air, when operating far from the wall, we estimate the Knudsen number Kn_2 based on cantilever half-width to be approximately 0.014. For most practical surfaces the molecular mean free path is comparable in magnitude to the slip length (Gad-El-Hak 2001), so that $L \approx Kn_2$. L is likely to be smaller in liquids (typically $L \approx 0.004$) provided the cantilever surface is smooth and uncontaminated (Cottin-Bizonne *et al.* 2005). Figure 9(a, b) in Appendix C shows how the drag on an unbounded circular cantilever when $L \lesssim 0.02$ differs from the no-slip value by an $O(L)$ amount, but in a frequency-dependent manner; recent boundary-element computations of unbounded oscillatory flow in a multiple-cantilever system (Ding & Wenjiig 2004) report the same order of magnitude for the drag correction. Slip effects are likely to be more important for cantilevers operating in either air or liquid very close to a substrate, when the drag (at least at sufficiently low frequencies) depends on L/Δ (the ratio of slip length to gap width). In liquids, slip lengths on hydrophobic surfaces of order 1 μm have been reported (Zhu & Granick 2001), possibly as a result of surface contamination (Cottin-Bizonne *et al.* 2005), and similarly large values can be anticipated for some coated or biological interfaces. Substrate-dependent slip can then have a leading-order effect on drag (as illustrated by figure 9c, d). For a cantilever very close to a substrate in air, the present model may lose its validity both through high values of slip and through discrete molecular effects (treated by Gallis & Torczynski 2004). The drag results presented here must therefore be interpreted with considerable caution in some circumstances, although the present results provide a foundation on which to base further studies.

Traditionally, thermal noise contamination is a hindrance to sampling in liquid environments. However, thermally excited cantilevers can be used to probe the micro-rheology of biological specimens. The nature of the technique means that the cantilever oscillates in close proximity to the substrate; the benefits of an increased understanding of wall effects in oscillatory Stokes flow are therefore clear (Ma, Jimenez & Rajagopalan 2000; Rajagopalan 2000). Even AFM techniques traditionally associated with quasi-steady flow (e.g. single-molecule measurements) are moving into territory where flow inertia could become non-negligible, through the development of

higher-speed modes of AFM operation designed to capture biology in real time and to counter effects such as sample drift during measurement. Under these circumstances existing quasi-steady models (e.g. Vinogradova *et al.* 2001; Alcaraz 2002) may need to be revised to take account of the unsteadiness issues addressed here.

This work was supported by EPSRC grant GR/R88991. We are grateful to Professor John Billingham for several helpful conversations.

Appendix A. Inviscid flow for $\gamma \gg 1$, $\gamma^{-1} \ll \Delta$

Here we consider the inviscid flow generated by high-frequency oscillations ($\gamma \gg 1$) of a circular cantilever when boundary layers are much thinner than the wall–cantilever distance ($\Delta \gg \gamma^{-1}$). In bipolar coordinates (3.1) the flow is governed by $\psi^{(0)}_{\xi\xi} + \psi^{(0)}_{\eta\eta} = 0$ subject to

$$\psi^{(0)}(\xi, 0) = 0, \quad \psi^{(0)}(0, \eta) = 0, \quad \psi^{(0)}(-\pi, \eta) = 0, \tag{A 1a}$$

$$\psi^{(0)}(\xi, \eta_1) = c \sin\xi/(\cosh\eta_1 - \cos\xi). \tag{A 1b}$$

We express $\psi^{(0)}$ as a Fourier series satisfying (A 1*a*),

$$\psi^{(0)} = \sum_{n=0}^{\infty} a_n \sinh n\eta \sin n\xi. \tag{A 2}$$

The coefficients a_n are determined by expressing the remaining boundary condition as

$$\sum_{n=1}^{\infty} a_n \sinh n\eta_1 \sin n\xi = \frac{c \sin\xi}{\cosh\eta_1 - \cos\xi} = 2c \sum_{n=1}^{\infty} \mathrm{e}^{-n\eta_1} \sin n\xi \tag{A 3}$$

($\eta_1 = \cosh^{-1}(1 + \Delta)$) which yields (4.20). The slip velocities on the cantilever surface and on the wall are then

$$u_c^s = \sum_{n=1}^{\infty} [(c - d_n)(n-1)e_{n-1} - (c + d_n)(n+1)e_{n+1} + 2d_n n e_n] \sinh n\eta_1 \sin n\xi, \tag{A 4a}$$

$$u_w^s = \sum_{n=1}^{\infty} [2ne_n - (n-1)e_{n-1} - (n+1)e_{n+1}] \sin n\xi, \tag{A 4b}$$

where $d_n = (1 + \Delta)/\tanh n\eta_1$ and $e_n = \mathrm{e}^{-n\eta_1}/\sinh n\eta_1$.

Appendix B. Inviscid flow for $\gamma \gg 1$, $\Delta \ll \gamma^{-1}$

When $\gamma \gg 1$, $\Delta \ll \gamma^{-1}$ the outer inviscid flow sees the cantilever as touching the wall (figure 8). In order to model this flow we employ the conformal mapping

$$\xi = -2x/(x^2 + y^2), \quad \eta = 2y/(x^2 + y^2). \tag{B 1}$$

Laplace's equation $\psi^{(0)}_{\xi\xi} + \psi^{(0)}_{\eta\eta} = 0$ must then be solved in the infinite strip $0 \leqslant \eta \leqslant 1$. In this new flow domain, $\eta = 0$ and $\eta = 1$ represent the wall and cantilever's surface, respectively, and $\xi = 0$ represents the vertical line of symmetry (see figure 8), giving the boundary conditions

$$\left.\begin{aligned} \psi^{(0)}(\xi, 0) = \psi^{(0)}(0, \eta) = 0, \quad \psi^{(0)}(\xi, 1) = -x = 2\xi/(\xi^2 + 1), \\ \psi^{(0)}(\xi, \eta) \to 2\eta/\xi \text{ as } \xi \to \infty. \end{aligned}\right\} \tag{B 2}$$

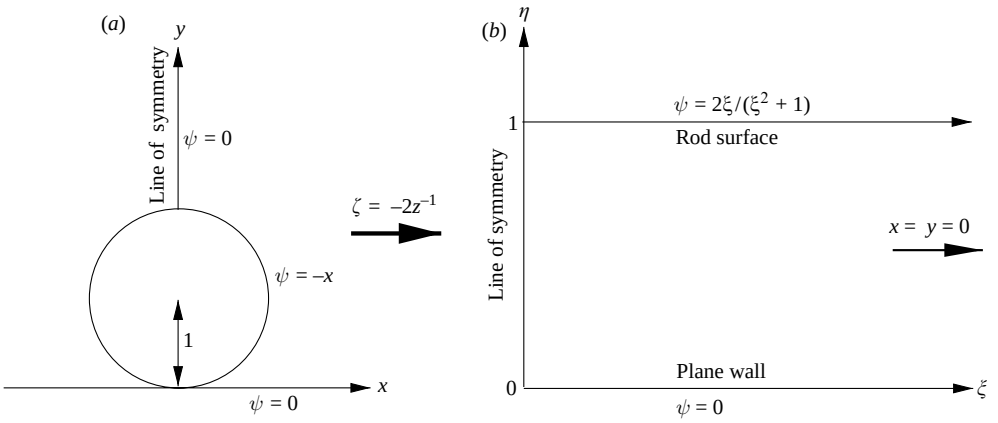

FIGURE 8. Conformal map $\zeta = -2z^{-1}$, $z = x + \mathrm{i}y$, $\zeta = \xi + \mathrm{i}\eta$ takes the flow domain for a circular cantilever touching a wall (*a*) into an infinite strip (*b*).

We express the streamfunction in the form

$$\psi^{(0)}(\xi, \eta) = 2\int_0^\infty A(k)\sinh 2\pi k\eta \sin 2\pi k\xi \,\mathrm{d}k, \tag{B 3}$$

which satisfies the homogeneous boundary conditions, and determine $A(k)$ by imposing the condition on the cantilever surface that

$$\psi^{(0)}(\xi, 1) = 2\int_0^\infty A(k)\sinh(2\pi k)\sin(2\pi k\xi)\,\mathrm{d}k = \frac{2\xi}{(\xi^2+1)} = 4\pi\int_0^\infty \mathrm{e}^{-2\pi k}\sin(2\pi k\xi)\,\mathrm{d}k, \tag{B 4}$$

which yields (4.35).

Appendix C. The effects of slip

To illustrate the implications of relaxing the no-slip condition, we revisit the cases of an unbounded circular cantilever (§ 4.2.1) and rectangular cantilever near a wall (§ 5.2.1), recalculating the drag using the Navier-slip condition (2.3).

C.1. *Unbounded circular cantilever* (*region VI/I*)

In streamfunction form, the flow is governed by (2.5*a*) subject to

$$u_r = \sin\theta, \quad u_\theta = L\frac{\partial}{\partial r}\left(\frac{u_\theta}{r}\right) + \cos\theta \tag{C 1}$$

on the cylinder surface $r = 1$, i.e.

$$\psi(1,\theta) = -\cos\theta, \quad -(1+L)\left.\frac{\partial\psi}{\partial r}\right|_{r=1} = -L\left.\frac{\partial^2\psi}{\partial r^2}\right|_{r=1} + \cos\theta, \tag{C 2}$$

with $\boldsymbol{u} \to \boldsymbol{0}$ as $r \to \infty$. This is satisfied by

$$\psi = \left(\frac{(CK_1(\sqrt{\mathrm{i}}\gamma) - 1)}{r} - CK_1(\sqrt{\mathrm{i}}\gamma r)\right)\cos\theta, \tag{C 3}$$

$$C = -\frac{(2+3L)}{\sqrt{\mathrm{i}}\gamma K_0(\sqrt{\mathrm{i}}\gamma)}\left(1 + L\left(\frac{2K_0(\sqrt{\mathrm{i}}\gamma) + \sqrt{\mathrm{i}}\gamma K_1(\sqrt{\mathrm{i}}\gamma)}{K_0(\sqrt{\mathrm{i}}\gamma)}\right)\right)^{-1}. \tag{C 4}$$

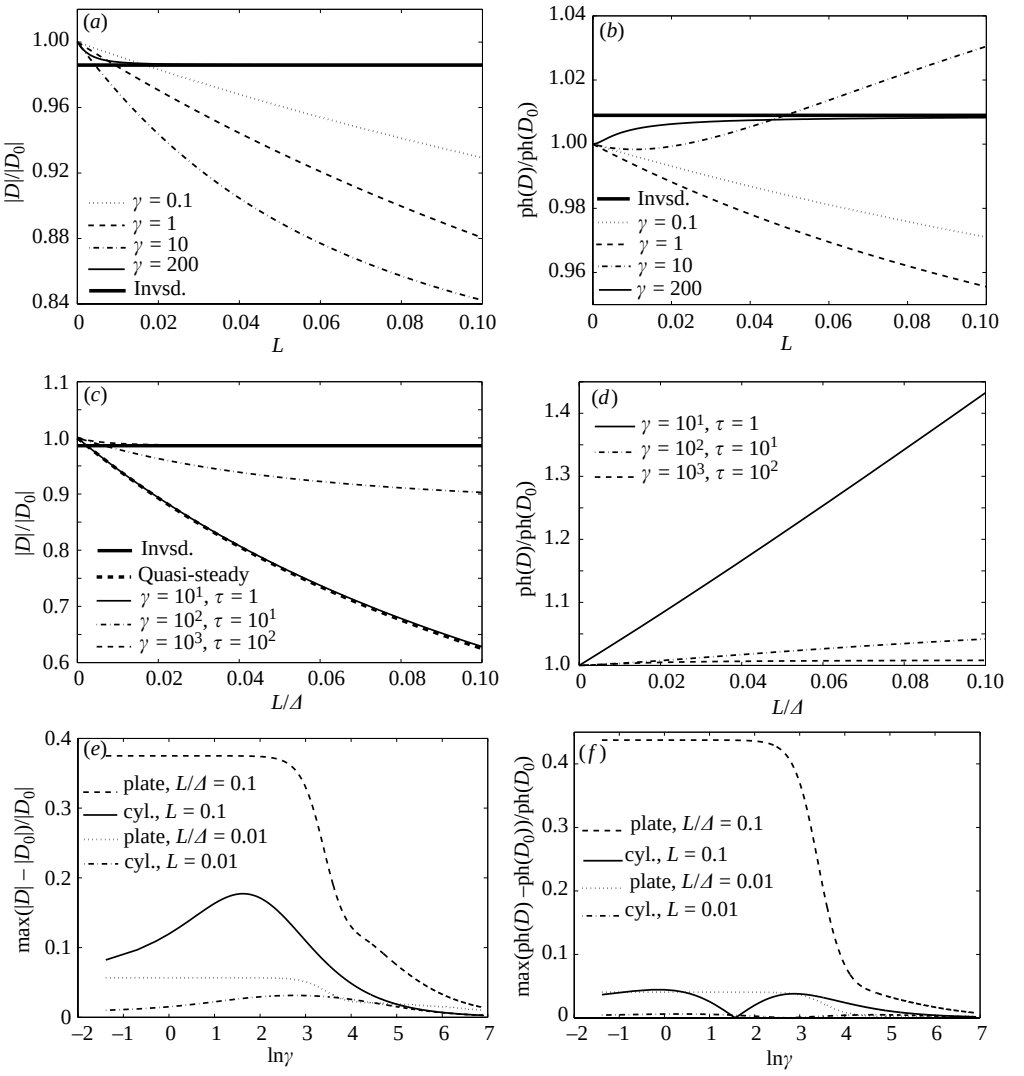

FIGURE 9. Variation in (a, c) amplitude and (b, d) phase of the drag (C 5, C 6) with slip length L (scaled on Δ in c and d), normalized on the no-slip value D_0: (a) and (b) relate to an unbounded cylinder oscillating at frequencies $\gamma = 0.1, 1, 10, 200$; (c) and (d) correspond to the lubrication drag on a plate oscillating near a wall when $\Delta = 10^{-1}$ and $\gamma = 10, 100, 1000$. Inviscid limits are shown with thick solid lines. The maximum deviation in the amplitude (e) and phase (f) of the drag are also plotted as a function of γ for two different L.

The drag is then found to be

$$D = -\mathrm{i}\pi\gamma^2(1 - 2CK_1(\sqrt{\mathrm{i}}\gamma)). \tag{C 5}$$

At leading order in L we recover the no-slip expression (4.15) and the high-frequency limit $\gamma \gg 1$ is dominated by the inviscid contribution $D_{inv} = -\mathrm{i}\pi\gamma^2$. The amplitude and phase of the drag are plotted in figure 9(a, b) respectively. For small γ the drag is almost linear in L and slip acts to decrease the amplitude and phase of the drag; however, these trends change at much larger γ. Initially the slip's influence increases with γ, yet after a point its impact declines, tending towards a largely slip-insensitive

inviscid limit. This phenomenon is displayed in figure 9(*e*, *f*), where it can be seen that there exists a non-zero γ which maximizes drag variations at a given slip length. We found that the frequency γ_0 which maximizes the reduction in drag amplitude satisfies $\gamma_0^{-2} \approx 0.4\,L$ (although we could not identify an equivalent relationship for the drag's phase).

C.2. *Rectangular cantilever in the lubrication limit* ($\tau \equiv \Delta\gamma = O(1)$, $\Delta \ll 1$)

Adopting (5.1), we can re-derive the lubrication drag on a rectangular cantilever with Navier-slip conditions on both the cantilever and nearby wall, assuming $\check{u} = \pm (L/\Delta)\partial\check{u}/\partial\check{y}$ on $\check{y} = (1 \mp 1)/2$. Following similar analysis as before gives the leading-order drag as

$$D = -\frac{2\alpha_+\gamma^3}{3\sqrt{\mathrm{i}}}\left(\sqrt{\mathrm{i}\tau}\alpha_+ + \mathrm{e}^{-\sqrt{\mathrm{i}\tau}} - 1 - \frac{(\alpha_+ + \alpha_-\mathrm{e}^{-\sqrt{\mathrm{i}\tau}})(\cosh\sqrt{\mathrm{i}\tau} - 1 + \sqrt{\mathrm{i}\tau}(L/\Delta)\sinh\sqrt{\mathrm{i}\tau})}{2\sqrt{\mathrm{i}\tau}(L/\Delta)\cosh\sqrt{\mathrm{i}\tau} + (1 + \mathrm{i}\tau^2(L/\Delta)^2)\sinh\sqrt{\mathrm{i}\tau}}\right)^{-1}, \quad \text{(C 6)}$$

where $\alpha_\pm = \sqrt{\mathrm{i}\tau}(L/\Delta) \pm 1$. For $(L/\Delta) \ll 1$,

$$D = \frac{2}{3}\mathrm{i}\Delta^{-3}\tau^2\left(\frac{\sqrt{\mathrm{i}\tau}\sinh\sqrt{\mathrm{i}\tau}}{2 - 2\cosh\sqrt{\mathrm{i}\tau} + \sqrt{\mathrm{i}\tau}\sinh\sqrt{\mathrm{i}\tau}}\right) + \frac{4}{3}\frac{L\Delta^{-4}\tau^4(1 - \cosh\sqrt{\mathrm{i}\tau})^2}{(2 - 2\cosh\sqrt{\mathrm{i}\tau} + \sqrt{\mathrm{i}\tau}\sinh\sqrt{\mathrm{i}\tau})^2} + O(L^2/\Delta^5). \quad \text{(C 7)}$$

At leading order we recover the no-slip result (5.2). When the gap separation is much smaller than the boundary-layer thickness ($\tau \ll 1$), (C 6) reduces to the quasi-steady limit $D = 8\Delta^{-3}/(1 + 6(L/\Delta))$ (cf. Vinogradova 1995). Alternatively, in the limit where boundary layers are much thinner than the separation distance ($\tau \gg 1$), the drag (C 6) tends to the inviscid limit $D_{inv} = \frac{2}{3}\mathrm{i}\gamma^2\Delta^{-1}$. In figure 9(*c*, *d*) we again see how slip influences the drag. As with the unbounded cylinder, at low γ the slip–drag relationship is essentially linear, becoming less so as γ is increased, until finally the inviscid limit is attained where slip matters little. Unlike the cylinder case, however, slip has its greatest influence in the quasi-steady limit, and only a weak effect at high γ (see figure 9*e*, *f*).

REFERENCES

Alcaraz, J. 2002 Correction of microrheological measurements of soft samples with atomic force microscopy for the hydrodynamic drag on the cantilever. *Langmuir* **18**, 716–721.

Avudainayagam, A. & Geetha, J. 1993 Oscillatory line singularities of Stokes' flows. *Intl J. Engng Sci.* **31**, 1295–1299.

Avudainayagam, A. & Geetha, J. 1995 Unsteady singularities of Stokes' flows in two dimensions. *Intl J. Engng Sci.* **33**, 1713–1724.

Avudainayagam, A. & Geetha, J. 1998 A boundary-integral equation for two-dimensional oscillatory Stokes flow past an arbitrary body. *J. Engng Maths* **33**, 251–258.

Basset, A. B. 1888 *A Treatise on Hydrodynamics*, vol. 2. Cambridge: Deighton Bell.

Benmouna, F. & Johannsmann, D. 2002 Hydrodynamic interaction of AFM cantilevers with solid walls: An investigation based on AFM noise analysis. *Eur. Phys. J.* E **9**, 435–441.

Blake, J. R. 1971 A note on the image system for a Stokeslet in a no-slip boundary. *Proc. Camb. Phil. Soc.* **70**, 303–310.

Blake, J. R. 1974 Singularities of viscous flow. Part II: Applications to slender body theory. *J. Engng Maths* **8**, 113–124.

Broday, M. 2002 Motion of nanobeads proximate to plasma membranes during single particle tracking. *Bull. Math. Biol.* **64**, 531–563.

Chon, J. W. M., Mulvaney, P. & Sader, J. E. 2000 Experimental validation of theoretical models for the frequency response of atomic force microscope cantilever beams immersed in fluids. *J. Appl. Phys.* **87** 3978–3988.

Chu, J. & Kim, M.-U. 2001 Two-dimensional oscillatory Stokes flows between two parallel planes. *Fluid Dyn. Res.* **29**, 7–24.

Chu, J. & Kim, M.-U. 2002 Two-dimensional oscillatory Stokes flow in the region with a semi-infinite plate parallel to an infinite plane wall. *Fluid Dyn. Res.* **31**, 229–251.

Chu, J. & Kim, M.-U. 2004 Oscillatory Stokes flow due to motions of a circular disk parallel to an infinite plane wall. *Fluid Dyn. Res.* **34**, 77–97.

Clarke, R. J., Jensen, O. E., Billingham, J. & Williams, P. M. 2005 Three dimensional flow due to a microcantilever oscillating near a wall: an unsteady slender-body analysis. *Proc. R. Soc. Lond.* A (submitted).

Cottin-Bizonne, C., Cross, B., Steinberger, A. & Charlaix, E. 2005 Boundary slip on smooth hydrophobic surfaces: intrinsic effects and possible artifacts. *Phys. Rev. Lett.* **94**, 056102.

Craig, V. & Neto, C. 2001 In situ calibration of colloid probe cantilevers in force microscopy: hydrodynamic drag on a sphere approaching a wall. *Langmuir* **17**, 6018–6022.

Davis, A. M. J. 1993 Some asymmetric Stokes flows that are structurally similar. *Phys. Fluids* A **5**, 2086–2094.

Ding, J. & Wenjiig, Y. 2004 A fast integral approach for drag force calculations due to oscillatory slip Stokes flow. *Intl J. Numer. Meth. Engng* **60**, 1535–1567.

Durlofsky, L. & Brady, J. F. 1987 Analysis of the Brinkman equations as a model for flow in porous media. *Phys. Fluids* **30**, 3329–3341.

Feng, J., Ganatos, P. & Weinbaum, S. 1998*a* The general motion of a circular disk in a Brinkman medium. *Phys. Fluids* **10**, 2137–2146.

Feng, J., Ganatos, P. & Weinbaum, S. 1998*b* Motion of a sphere near planar confining boundaries in a Brinkman medium. *J. Fluid Mech.* **375**, 265–296.

Finn M. D. & Cox, S. M. 2001 Stokes flow in a mixer with changing geometry. *J. Engng Maths* **41**, 75–99.

Gad-El-Hak, M. 2001 Flow physics in MEMS. *Mec. Ind.* **2**, 313–341.

Gallis, M. A. & Torczynski, J. R. 2004 An improved Reynolds-equation model for gas damping of microbeam motion. *J. Microelectromech. Sys.* **13**, 653–659.

Hall, P. & Papageorgiou, D. T. 1999 The onset of chaos in a class of Navier–Stokes solutions. *J. Fluid Mech.* **393**, 59–87.

Jeffery, G. B. 1921 Plane stress and plane strain in bipolar coordinates. *Phil. Trans. R. Soc. Lond.* A **221** 265–293.

Jeffrey, D. J. & Onishi, Y. 1981 The slow motion of a cylinder next to a plane wall. *Q. J. Mech. Appl. Maths* **34**, 129–137.

Kanwal, R. P. 1955 Vibrations of elliptic cylinders and a flat plate in a viscous fluids. *Z. Angew. Math. Mech.* **35** 17–22.

Kim, M.-U., Kim, K. W., Cho, Y.-H. & Kwak, B. M. 2001 Hydrodynamic force on a plate near the plane wall. Part II: plate in squeezing motion. *Fluid Dyn. Res.* **29**, 171–198.

Kim, S. & Russel, W. B. 1985 The hydrodynamic interactions between two spheres in a Brinkman medium. *J. Fluid Mech.* **154** 253–268.

Lawrence, C. J. & Weinbaum, S. 1986 The force on an axisymmetric body in linearized time-dependent motion: a new memory term. *J. Fluid Mech.* **171** 209–218.

Lawrence, C. J. & Weinbaum, S. 1988 The unsteady force on a body at low Reynolds number; the axisymmetric motion of a spheroid. *J. Fluid Mech.* **189**, 463–489.

Liron, N. & Blake, J. R. 1981 Existence of viscous eddies near boundaries. *J. Fluid Mech.* **107**, 109–129.

Loewenberg, M. 1993 The unsteady Stokes resistance of arbitrarily oriented, finite-length cylinders. *Phys. Fluids* A **5**, 3004–3006.

Loewenberg, M. 1994*a* Asymmetric, oscillatory motion of a finite-length cylinder: The macroscopic effect of particle edges. *Phys. Fluids* **6**, 1095–1107.

Loewenberg, M. 1994*b* Axisymmetric unsteady Stokes flow past an oscillating finite-length cylinder. *J. Fluid Mech.* **265**, 265–288.

Lovalenti, P. & Brady, J. F. 1993 The hydrodynamic force on a rigid particle undergoing arbitrary time-dependent motion at small Reynolds number. *J. Fluid Mech.* **256**, 561–605.

Ma, H., Jimenez, J. & Rajagopalan, R. 2000 Brownian fluctuation spectroscopy using atomic force microscopes. *Langmuir* **16**, 2254–2261.

Nnebe, I. & Schneider, J. W. 2004 Characterization of distance-dependent damping in tapping-mode atomic force microscopy force measurements in liquid. *Langmuir* **20**, 3195–3201.

Paul, M. R. & Cross, M. C. 2004 Stochastic dynamics of nanoscale mechanical oscillators immersed in a viscous fluid. *Phys. Rev. Lett.* **92**, 235501.

Pozrikidis, C. 1989*a* A singularity method for unsteady linearized flow. *Phys. Fluids* **9**, 1508–1520.

Pozrikidis, C. 1989*b* A study of linearized oscillatory flow past particles by the boundary-integral method. *J. Fluid Mech.* **202**, 17–41.

Pozrikidis, C. 1992 *Boundary Integral and Singularity Methods for Linearized Viscous Flow*. Cambridge University Press.

Pozrikidis, C. 1996 *Introduction to Theoretical and Computation Fluid Dynamics*. Oxford University Press.

Rajagopalan, R. 2000 Atomic force and optical force microscopy: applications to interfacial microhydrodynamics. *Colloids Surfaces* **174**, 253–267.

Riley, N. 2001 Steady streaming. *Annu. Rev. Fluid Mech.* **33**, 43–65.

Rosenhead, L. 1963 *Laminar Boundary Layers*. Clarendon.

Roy, S., Raju, R., Chuang, H. F., Cruden, B. A. & Meyyappan, M. 2003 Modeling gas flow through microchannels and nanopores. *J. Appl. Phys.* **93**, 4870–4879.

Russel, W. B., Hinch, E. J., Leal, L. G. & Tieffenbruck, G. 1977 Rods falling near a vertical wall. *J. Fluid Mech.* **83**, 273–287.

Sader, J. E. 1998 Frequency response of cantilever beams immersed in viscous fluids with applications to the atomic force microscope. *J. Appl. Phys.* **84**, 64–76.

Santos, N. C. & Castanho, M. A. R. B. 2004 An overview of the biophysical applications of atomic force microscopy. *Biophys. Chem.* **107**, 133–149.

Secomb, T. W. 1978 Flow in a channel with pulsating walls. *J. Fluid Mech.* **88**, 273–288.

Smith, S. H. 1987 Unsteady Stokes' flow in two dimensions. *J. Engng Maths* **21**, 281–285.

Smith, S. H. 1993 Unsteady separation for Stokes flow in two dimensions. *Phys. Fluids* A **5**, 1095–1104.

Smith, S. H. 1995 Structural changes in transient Stokes flow. *Q. J. Mech. Appl. Maths* **48**, 285–309.

Smith, S. H. 1997 Slow oscillatory Stokes flow. *Q. Appl. Maths* **55**, 1–22.

Stokes, G. G. 1851 On the effect of the internal friction of fluids on the motion of pendulums. *Trans. Camb. Phil. Soc.* **9**, 182–187.

Stuart, J. T., DiPrima, R. C., Eagles, P. M. & Davey, A. 1990 On the instability of the flow in a squeeze lubrication film. *Proc. R. Soc. Lond.* A **430**, 347–375.

Sugihara-Seki, M. 2004 Motion of a sphere in a cylindrical tube filled with Brinkman medium. *Fluid Dyn. Res.* **34**, 59–76.

Tekasakul, P., Tompson, R. V. & Loyalka, S. K. 1998 Rotary oscillations of arbitrary axi-symmetry bodies in an axi-symmetric viscous flow: numerical solutions. *Phys. Fluids* **10**, 2797–2818.

Thompson, P. A. & Troian, S. M. 1997 A general boundary condition for liquid flow at solid surfaces. *Nature* **389**, 360–362.

Tuck, E. O. 1964 Some methods for flows past blunt slender bodies. *J. Fluid Mech.* **18**, 619–635.

Tuck, E. O. 1969 Calculation of unsteady flow due to small motions of cylinders in a viscous fluid. *J. Engng Maths* **3**, 29–44.

Vinogradova, O. I. 1995 Drainage of a thin liquid film confined between hydrophobic surfaces. *Langmuir* **11**, 2213–2220.

Vinogradova, O. L., Butt, H., Yakubov, G. E. & Feuillebois, F. 2001 Dynamics effects on force measurements I. Viscous drag on the atomic force microscope cantilever. *Rev. Sci. Instrum.* **72**, 2330–2339.

Watson, E. B. B., Banks, W. H. H., Zaturska, M. B. & Drazin, P. G. 1990 On transition to chaos in two-dimensional channel flow symmetrically driven by accelerating walls. *J. Fluid Mech.* **212**, 451–485.

Zhang, W. & Stone, H. A. 1998 Oscillatory motions of circular disks and nearly spherical particles in viscous flows. *J. Fluid Mech.* **367**, 329–358.

Zhu, Y. & Granick, S. 2001 Rate-dependent slip of Newtonian liquid at smooth surfaces. *Phys. Rev. Lett.* **87**, 096105.